https://doi.org/10.5194/wes-2025-36
Preprint. Discussion started: 8 April 2025

eawe european academy of wind energy
Open Access
WIND ENERGY SCIENCE DISCUSSIONS

On the mitigation of detrimental effects via passive flow-control devices in small-scale horizontal-axis wind-turbines operating under turbulence and surface degradation effects

Ander Zarketa-Astigarraga[1], Uxue Arrieta-Lizarazu[1], Makel Penalba[1,2], Alain Martin-Mayor[1], and Manex Martinez-Agirre[1]

[1]Mondragon Unibertsitatea, Faculty of Engineering, Mechanical and Industrial Production, Loramendi 4, Mondragon 20500 Gipuzkoa, Spain
[2]Ikerbasque, Basque Foundation for Science, Euskadi Plaza 5, 48011 Bilbao, Spain

Correspondence: Ander Zarketa-Astigarraga (azarketa@mondragon.edu)

Abstract. Small-scale horizontal axis wind turbines (SHAWTs) installed in distributed grids are increasingly important for achieving net-zero emissions by minimizing visual and environmental impacts. However, the understanding of SHAWTs under combined turbulence and roughness conditions, operating at chord-based transitional Reynolds numbers ranging from 1×10^5 to 5×10^5, is still limited. This study examines the combined influence of environmental turbulence and surface degradation on a transitionally-operating NACA0021 airfoil equipped with passive flow-control devices (PDs) to mitigate detrimental effects. Results show that specific *PD* distributions can delay stall up to 5° and reduce performance loss by enhancing the aerodynamic efficiency up to 16% under certain flow conditions.

Using experimental data, the study estimates the annual energy production (AEP) of a standard 7.8 kW-rated SHAWT using a blade-element method code. Simulations reveal that, when SHAWT blades are affected by turbulence and surface degradation along their entire span, certain *PD* distributions can enhance the AEP by up to 80% compared to their bare counterparts. These findings highlight the potential of *PD*s in enhancing SHAWT's performance and the importance of pitch-regulated control in mitigating adverse effects.

1 INTRODUCTION

1.1 Context and motivation

The rising interest in renewable energies as alternatives to fossil fuels is reflected in the global trends of the wind energy industry. Notably, in 2022, the sector witnessed a surge with 77.6 GW of installed capacity worldwide, almost reaching the milestone of 1 TW in operation (Zhao and Hutchinson, 2023). This achievement is a significant leap from the 825 MW of globally installed wind power reported in 2022, indicating a substantial increase in wind-turbine deployment (202, 2022).

The remarkable expansion in power capacities can largely be attributed to a technological strategy centered around constructing larger turbines. Compared to the wind turbines of the 1980s, modern versions boast rotor blade diameters up to 8 times larger, reaching up to 20MW in the largest offshore version (Ashuri et al., 2016), which serves as a primary means of enhancing power output (Amirzadeh et al., 2017).

Nonetheless, it's crucial to note that the LSWT sector is not the only player in the wind industry landscape. Recently, the small-scale wind turbine (SSWT) sector has been gaining relevance (Bianchini et al., 2022). The American Wind Energy Association defines SSWTs as turbines with a rated power of up to 100 kW and a maximum rotor diameter of 20 meter (201, 2010). Although the capacity of SSWTs may seem modest compared to the multi-megawatt output and over 100-meter-long diameters of current LSWTs, their recent growth and widespread adoption require special attention.

Governments in the US and European countries have been actively promoting policies to encourage the integration of electric power from SSWTs. The goal of such policies is to advance self-sufficient and decentralized power generation systems, aligned with the European Union's green deal strategy (Ruggiero et al., 2015; Moreira Chagas et al., 2020; Torres-Madroñero et al., 2020). The appeal of self-sufficiency is driven by environmental concerns such as global warming and the visual impact of large turbines. Within the context of net-zero-emission agreements by 2050 in the LSWT sector, investments in the small-scale industry are seen as a complementary approach to achieving environmental goals, especially in urban and isolated environments where deploying SSWT-based distributed grids can have a reduced environmental impact (Torres-Madroñero et al., 2020).

The global installed capacity for SSWTs has reached 950 MW, indicating a substantial increase, with the sector experiencing a growth rate of over 50% during 2013-2018 (Moreira Chagas et al., 2020; Bianchini et al., 2022).

1.2 The role of the boundary-layer upon transition

The dimensional reduction of the devices makes their blades operate at much lower Reynolds numbers (Tummala et al., 2020; Arumugam et al., 2021), which may range between 50k and 500k in case of small-scale horizontal-axis wind-turbine (SHAWT) blade designs (Arumugam et al., 2021; Hamlaoui et al., 2022). The flow under such Reynolds numbers is known to be transitional, developing complex aerodynamic structures upon its surface (Karthikeyan et al., 2014; Ananda et al., 2015; Du et al., 2015; Meng et al., 2018; Cho, 2019; Zarketa-astigarraga et al., 2022).

The complexity of the flow arises from the instabilities that grow within the boundary-layer developed along the airfoil surface. The fundamentals of boundary-layer theory may be found elsewhere, with the canonical work of Schlichting being a referential one (Schlichting and Gersten); the notions that follow are a synthesis of the fundamentals described there. The boundary-layer refers to the portion of the flow close to the surfaces of a body in which the viscous effects become as relevant as the convective ones, with the viscosity of the fluid decelerating the flow until fulfilling the boundary-condition of a null relative velocity at the wall, known as the no-slip condition. The ratio between the orders of magnitude of the convective and viscous forces is the governing parameter of the boundary-layer evolution, and is termed the Reynolds number. The Reynolds number is defined as $\mathrm{Re} = \rho V L/\mu$, with ρ and μ being the density and viscosity of the fluid respectively, and thus dependant on the medium. Besides, V and L are the characteristic velocity and length of the system being considered, and are thus application-specific.

The regime of the boundary-layer depends on the order of magnitude that the Reynolds value adopts, apart from being case-specific. For external flows such as air streams around airfoils, the boundary-layers may be classified as laminar or turbulent.

Laminar boundary-layers are those for which the ratio between convective and viscous forces is small enough, i.e. Re $\leq 10^4$. Under such conditions, the viscous force is large enough for damping any instability within the layer, and the flow close to the wall evolves in staggered layers that act upon each other by shear stresses; hence the term “laminar” for describing the flow. On the other hand, when Re $\geq 5 \times 10^5$, it can be assumed that the kinetic energy of the flow is large enough for overcoming the damping effect of viscosity. Any perturbation within the boundary-layer gets amplified, and the resultant flow does not evolve in an orderly manner as in the laminar regime. Instead, turbulent eddies are formed within the layer, with their mutual interactions becoming stronger with the development of the flow along the surface.

By particularizing the Navier-Stokes equations for a boundary-layer developed upon a flat-plate, and performing an estimation upon the orders of magnitude of the different terms, Schlichting already showed that several parameters characterizing the layer correlate differently with the Reynolds number depending on the regime of the flow (Schlichting and Gersten). For the purposes of the present work, suffices to say that the thickness of a laminar boundary-layer, namely δ, evolves as $\delta \propto \mathrm{Re}_x^{-1/2}$, where the subscript x refers to the streamwise location at which the Reynolds number is calculated (i.e. $\mathrm{Re}_x = \rho V x/\mu$). In the case of a turbulent boundary-layer, the dependence is $\delta \propto \mathrm{Re}_x^{-1/5}$. Such dependencies also apply to the skin-friction coefficient of the surface, which is directly related to the drag force experienced by the considered body.

The notions described above, although developed for a flat-plate configuration, may be qualitatively applied to an airfoil. In such a case, the Reynolds number that determines the regime of the flow is calculated by considering the chordal dimension as the characteristic length, $\mathrm{Re}_c = \rho V c/\mu$. If such a number falls in the laminar regime, the boundary-layer will sustain a laminar behavior throughout the surface of the airfoil, departing from the leading-edge and thickening while it flows along the chordal dimension as $\mathrm{Re}_x^{-1/2}$. The same reasoning applies in the case Re_c is turbulent.

However, it may happen that the Reynolds number does not fall within any of the regimes described above, but in between. That is what occurs in the case $1 \times 10^4 \leq \mathrm{Re}_c \leq 5 \times 10^5$, which is known as the transitional regime. In that case, the boundary-layer begins as a laminar structure at the leading-edge of the airfoil, but due to the amplification of the instabilities that develop within, it may eventually turn into a turbulent one. The passage from a laminar to a turbulent boundary-layer is called transition, a complex phenomenon driven by different mechanisms depending on the freestream conditions of the flow and the surface roughness of the body. Plenty of literature may be found on the role of different freestream and roughness parameters upon the mechanism of transition, with the review of Reshotko being a classical reference on the field (Reshotko). What is relevant for the research undertaken herein is that transition may occur in two ways: either naturally, leaving the instabilities of the boundary-layer evolve without any external perturbations. Or forcing such instabilities, causing what is called as bypass transition.

The natural transition mechanism was thoroughly described and conceptualized by Gaster in a series of papers (Gaster, 1965, 1967, 1968). According to this view, the instabilities that grow within the laminar boundary-layer, when surpassing a given amplification threshold, make the flow separate from the surface. The separated boundary-layer, which adopts the form of a shear-layer, undergoes transition and becomes turbulent. If the surface of the body is close enough once transition is completed, the energized layer reattaches to the body, and flows downstream in the form of a turbulent boundary-layer. The chordal extent that spans between the separation and reattachment regions constitutes a structure of a recirculating, relatively

https://doi.org/10.5194/wes-2025-36
Preprint. Discussion started: 8 April 2025

low-speed flow. Such a structure is called a laminar separation bubble (LSB), and is known to be highly sensitive to the freestream conditions (especially the Reynolds number and the angle-of-attack) and the surface roughness. If those conditions are harsh enough, such as high turbulence levels or a coarse surface roughness, the boundary-layer gets perturbed in excess and the laminar portion is swept away. The corresponding mechanism, in which no LSB structures are present, is called bypass transition.

The influence of freestream turbulence and surface roughness on the transitional structures formed upon a NACA0021 airfoil have been investigated by the authors in previous studies (Zarketa-Astigarraga et al., 2021; Zarketa-astigarraga et al., 2022). The trends observed suggest that the LSB gets reduced with increasing Reynolds number, and that it moves towards the leading-edge with higher angles-of-attack. Those two modifications, the shrinking of the bubble and its upwards motion, make the portion of the turbulent boundary-layer larger. The straightforward effect of such a mechanism is to increase the drag upon the airfoil, which may induce the power reduction on a turbine equipped with blades operating under such conditions. The lift load also gets affected, following the same trend as the drag. The presence of turbulence and roughness accentuate such a behavior, as they promote the transition mechanism and, hence, the length of the turbulent boundary-layer. The purpose of the present paper is to devise and implement some flow-control technique to mitigate such effects, as mentioned below.

1.3 Wind-turbines under environmentally perturbing agents

Due to their different installation sites of the turbines, the operating conditions of SSWTs can vary significantly with respect to LSWTs (Torres-Madroñero et al., 2020). Transitionally-operating airfoils cover diverse applications. For instance, studies on the role of surface roughness on both the thermal and the aerodynamic behaviour of turbomachinery vanes have resulted on a considerable bibliographical corpus, as synthesized by Bons (Bons). The review summarizes the open literature of the past 70 years, and draws two main conclusions that are worth considering. First of all, that surface roughness may play a positive role on the thermal behaviour of gas turbine vanes, enhancing the heat transfer and reducing the thermal stresses accordingly; however, such a role may turn detrimental in terms of aerodynamic efficiency, as it promotes transition and the development of turbulent boundary-layers that augment the drag forces. Nonetheless, the relevance of the thermal and aerodynamic effects are acknowledged to be highly dependent on the Reynolds number, especially on the transitional regime. Secondly, that the revisited literature shows a clear lack of consensus when it comes to identifying the parameters required for characterizing the surface roughness, as well as an absence of a unified protocol for undertaking tests under such conditions. Hence, the revision asserts, more research is necessary for understanding the physical mechanisms at play. More recent studies on the topic show advances on the weak aspects outlined by Bons, although the improvements seem to be highly application-specific and not easily extrapolated to other fields such as the wind-turbine ones (Flack et al.; Zamiri et al.).

Another common application that deals with transitionally-operating airfoils is the one concerned with the aerodynamics of micro and unmanned aerial vehicles, respectively termed MAVs and UAVs. If turbomachinery vanes constitute an application in which surface roughness effects play a relevant role, MAV and UAV devices may be considered to be affected, largely, by atmospheric turbulence. Two referential works on this respect are those of Watkins et al. (Watkins et al., b) and Thompson & Watkins (Thompson et al.). They show that devices operating within the atmospheric boundary-layer (ABL) are subjected to a highly turbulent flow, and that such eddies affect the aerodynamic behaviour of the wings in terms of stability and control. As occurs in the case of surface roughness effects, turbulence depends on the Reynolds number, as well as being an application-specific mechanism. Indeed, MAV and UAVs are shown to be affected in a different manner depending on the relative scale of the eddies to the chordal dimension of the wings. The effect is shown to be enhanced when both lengths are of the same order of magnitude, with freestream fluctuations promoting an earlier boundary-layer transition. Such a promotion, although suppressing detrimental aerodynamic structures such as the LSB, may induce a loss of stability of the vehicle, requiring a more robust control strategy for overcoming the effects. As mentioned before for the surface-roughness aspect, more recent studies have shed light upon the turbulent effects (Watkins et al., a), although care should be taken when transferring those conclusions to other fields.

Grounding the analysis on the wind-turbine sector, it is clear that the two phenomena mentioned so far may affect the devices differently depending on the scale of the turbines. Both turbulence and roughness will play a role in devices that operate within the ABL and that are subject to potential surface damage by environmental agents such as rain, insects, dust or ice. The turbulent nature of urban and isolated rural environments is an acknowledged fact, with turbulence intensities reaching values in the range 29-34% depending on the terrain and orography of the environment (KC et al., 2019; Kc et al., 2020). The effect of increased turbulence levels upon the power production of the turbine does not seem to have reached a univocal consensus: there are studies pointing towards an increase of such a production with higher levels of turbulence, either at the rotor (Kc et al., 2020; Wekesa et al., 2016) or at the blade level of SHAWTs (Maldonado et al., 2015); however, such an increase is reported to be highly dependent on the flow conditions, with the correlation between turbulence and power outcome being liable to revert at high wind speeds (Maldonado et al., 2015). Regardless of the exact interrelation between those parameters, the fact that turbulence increase induces higher fatigue loads and lower life expectancy seems to be better established and accepted (Kc et al., 2020; Wekesa et al., 2016; Maldonado et al., 2015), an issue that poses major problems in such isolated environments where the availability of maintenance and reparation resources is scarce (Martini et al., 2016). When it comes to roughness effects, blade surface degradation is reported to downgrade the aerodynamic behaviour severely (Corten and Veldkamp, 2001; Khalfallah and Koliub, 2007; Sareen et al., 2013; Han et al., 2018; Latoufis et al., 2019; Torres-Madroñero et al., 2020; Curci et al., 2021), even reaching to halve the power outcome of the turbines (Corten and Veldkamp, 2001). Despite the diversity of degradation-inducing agents, which cover configurations that go from sand particle accumulation in desertic areas (Khalfallah and Koliub, 2007) to rain-induced erosion (Bartolomé and Teuwen, 2019; Mohamed Elhadi and Mamoun, 2020; Law and Koutsos, 2020), the studies agree on acknowledging that the critical region stands at the leading-edge of the airfoils, and that the degraded blades have a negative effect on the power production of the turbine. Even if such an effect is highly dependent on the type of turbine and the degradation level of the blades, annual energy production (AEP) losses are estimated to grow up to about 4% (Han et al., 2018). In the case of SHAWTs, those losses need to be considered jointly with the additional handicap of the acoustic noise emitted by the degraded blades (Latoufis et al., 2019), turning roughness into a mandatory factor to be studied together with turbulence.

1.4 Performance and AEP issues: the need for flow-control techniques

The literature revisited above shows the necessity of understanding the combined effect of turbulence and roughness upon transitionally-operating airfoils employed in wind-turbine blades. On this respect, two previous studies of the authors may be mentioned. The first one shows that the dependence of the aerodynamic behaviour of the airfoil on the external flow conditions gets accentuated in the transitional regime, with lift and drag variations being detectable at Reynolds increments as low as 20k (Zarketa-astigarraga et al., 2022). The second acknowledges that turbulent and roughness effects interplay synergistically within the transitional regime, inducing higher losses than when considering their individual effects separately, and downgrading the aerodynamic efficiency of the airfoil over 60% in the worst-case scenario, when compared against the same efficiency obtained for the clean flow paradigm at the design angle-of-attack (Zarketa-Astigarraga et al., 2023). The study analyzes the AEP evolution of a 7.8 kW-rated SHAWT, and shows that the turbulent scenario causes a 38% decrease on the annual outcome, whereas the combined effect induces a loss beyond 44%. Apart from the mandatory nature of including both turbulence and roughness effects on a thorough aerodynamic analysis of turbine blades, the work shows the need for undertaking certain actions in order to restore the aerodynamic behaviour of undamaged airfoils. One of such actions goes through repairing the blades periodically, a common approach that, nonetheless, incurs in high operation and maintenance (O&M) costs or may suffer from accessibility limitations (Martini et al., 2016; Orrell et al., 2018; Mishnaevsky, 2019; Torres-Madroñero et al., 2020). In the case of SHAWTs, a typical estimate of such costs raises up to $43/kW/year (Orrell et al., 2018; Torres-Madroñero et al., 2020), a non-negligible surcharge that may lead the turbine designers to prefer a preventive O&M strategy based on monitoring and controlling the blades, reducing the losses that roughness effects induce on the power production.

On this respect, flow-control techniques may constitute a loss mitigation strategy that needs to be considered. Those techniques can be diverse in nature, although a typical grouping classifies them under active and passive methods. The active ones require an external energy source for functioning, and comprise approaches such as plasma dischargers (Yarusevych and Kotsonis, 2017; Hultgren and Ashpis, 2018; Meng et al., 2018), micro-electro-mechanical devices (Ricci et al., 2011; Panta et al., 2018) or acoustic waves (Ricci et al., 2007; Ricci and Montelpare, 2009); although they provide a high versatility for covering a wide range of incoming flow conditions, the systems themselves are complex to implement, and may not always prove as useful as in LWTs due to the requirement of employing part of the power production of the SHAWTs for driving the control devices. On the other hand, passive techniques do not require such an external input and their installation is relatively straightforward, although their versatility is lower than what their active counterparts show; superhydrophobic coatings (Kok and Young, 2014; Chini et al., 2017), riblet-shaped films (Dean and Bhushan, 2010; Sareen et al., 2013) or devices such as vortex generators (Shahinfar et al., 2012; Mueller-Vahl et al., 2012; Hansen et al., 2015; Gao et al., 2015) are paradigmatic examples of passive techniques. In spite of the variety of approaches aiming at flow-control, the underlying mechanisms on which they operate are similar: either they try to act upon the flow for delaying stall, providing a wider interval of sustained lift and reduced drag (Yarusevych and Kotsonis, 2017; Hultgren and Ashpis, 2018; Meng et al., 2018; Shahinfar et al., 2012; Mueller-Vahl et al., 2012; Hansen et al., 2015; Gao et al., 2015; Ricci et al., 2007; Ricci and Montelpare, 2009); or they attempt at reducing the drag penalty in order to gain efficiency points (Kok and Young, 2014; Chini et al., 2017; Dean and Bhushan, 2010; Sareen et al., 2013). The upshot is that flow-control techniques can improve the aerodynamic behaviour of the blades, with its corresponding mitigation of AEP losses.

The study herein is a continuation of a previous work initiated by the authors (Zarketa-astigarraga et al., 2022; Zarketa-Astigarraga et al., 2023). The combined turbulence and roughness effects seem to be attracting the attention of researches lately, especially in LSWT systems (Ozçakmak et al.; Li et al.). However, more research effort is still required in the SSWT sector. Given the negative synergies between turbulence and roughness, identified and exposed by the authors in (Zarketa-Astigarraga et al., 2023), the effectiveness of the control techniques needs to be revisited for flow configurations that consider the effects of environmentally perturbing agents.

On this respect, the study pursues two specific goals by showing the capability of a particular control technique, namely a passive-device-based (*PD*) approach, for:

- improving the aerodynamic behaviour of airfoils employed in a specific SHAWT system subjected to the combined effect of turbulence and roughness.
- Estimating the reduction in AEP loss of such a system due to the implementation of the control technique.

For such a purpose, the undertaken analysis relies on a number of assumptions:

- the stress is put on the effect that the *PD*s have on previously determined aerodynamic characteristics of a NACA0021 airfoil subjected to turbulent and roughness effects (Zarketa-Astigarraga et al., 2023).
- The parameters analyzed are of global nature, namely the evolutions of lift (c_l) and drag (c_d) coefficients with the angle-of-attack (α). In this first approximation, no attempts are made to consider the influence of local flow structures, such as the variations of the transition location, on the overall system. This assumption does not imply that the transitional regime should not be analyzed further. It means that transitional effects will be sought, exclusively, in terms of the variations that the $c_l - \alpha$ and $c_d - \alpha$ curves show.
- The NACA0021 airfoil is used as the baseline geometry for building up a virtual model of a 7.8 kW-rated SHAWT, following the same procedure as in (Zarketa-Astigarraga et al., 2023). The resultant wind-turbine does not replicate a real-world device in full detail, as these, typically, use airfoil geometries other than the NACA0021 employed herein. However, measurements upon the NACA0021 have been validated before (Zarketa-Astigarraga et al., 2021; Zarketa-astigarraga et al., 2022), and the aim of the study is to transfer the sanctioned validity of such measurements to the AEP loss estimations of the SHAWT. Once the overall procedure is validated, the research program will proceed by considering airfoil geometries employed in real-world devices.
- The choice of *PD*s as a flow-control technique is based on its simplicity and easiness of implementation. The purpose is to determine whether the notion of flow-control, applied to transitionally-operating airfoils subjected to turbulence

https://doi.org/10.5194/wes-2025-36
Preprint. Discussion started: 8 April 2025

and roughness flow conditions, has any feasibility at all. However, the employment of *PD*s by no means constitutes an assertion of preference from the authors. Instead, it is a call to other researchers for studying the feasibility of additional control techniques upon transitionally-operating airfoils, after having shown the enhancing potential of one such methods.

Once such an enhancing potential is ruled out, the obtained $c_l - c_d$ relations, or aerodynamic polars, are extrapolated for estimating the AEP loss reductions of a common SHAWT design by means of a blade-element-momentum-based (BEM) code. For illustrative purposes, the twofold experimental-numerical framework described above is schematically represented in Figure 1, which highlights a methodology that is similar to the one presented in a previous work by the authors (Zarketa-Astigarraga et al., 2023), with the addition of the *PD*-based flow-control approach.

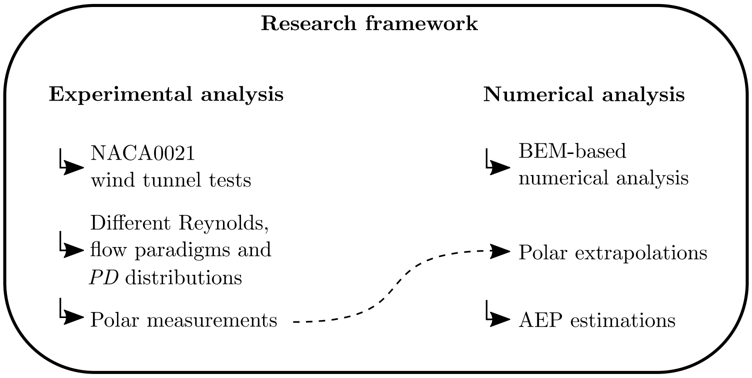

Figure 1. Schematic framework of the research.

Thus, the rest of the paper is organized in the following manner: Section 2 details the overall framework of the work, presenting both the wind tunnel set-up employed for the experiments and the numerical configuration by which the AEP losses are estimated. Section 3 specifies the particular SHAWT employed as a case-study for the AEP loss estimations. Section 4 presents the results and deals with the corresponding discussions. Section 5 summarizes the main contributions of the work, and provides some guidelines for future research lines.

2 Research framework

The workflow outlined in Figure 1 is constituted by the two main approaches described below: Section 2.1 deals with the experimental part, detailing the particularities of the wind tunnel and measurement protocols, and Section 2.2 prescribes the guidelines followed in the numerical approach.

https://doi.org/10.5194/wes-2025-36
Preprint. Discussion started: 8 April 2025

2.1 Experimental analysis of the blade response

The estimation of a SHAWT's AEP losses due to its exposure to combined turbulent and rough flow conditions requires determining the response of its blades, which comprise the main power production mechanism of the system, under those same flow conditions. The experimental set-up and methodology accounting for such an aerodynamic study are detailed in what follows.

2.1.1 Experimental set-up

An open-circuit wind tunnel driven by a 37 kW fan is employed for the experiments. The facility owns a rectangular cross-section of 0.75×1 m^2 and a 3-meter-long test-section, being capable of producing flows with peak velocities of 40 m/s and turbulence levels below 0.2%. Detailed information on the tunnel and its flow-related quality parameters can be found in (Torrano, 2016; Zarketa-Astigarraga et al., 2020a). Figure 2a provides a schematic draft of the set-up.

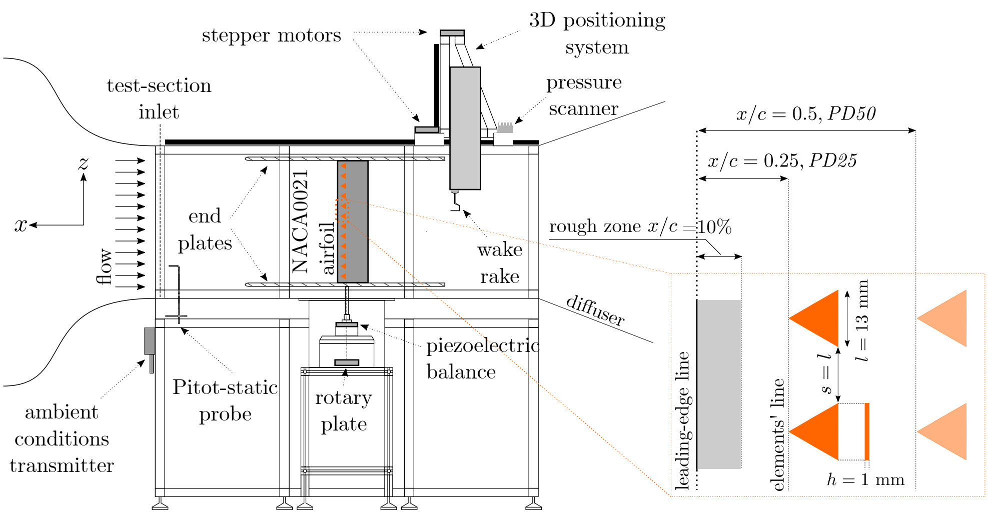

(a) (b)

Figure 2. (a): Schematic illustration of the wind tunnel set-up for undertaking measurements upon a *PD*-equipped airfoil; (b): the employed generic distribution of *PD*s.

The NACA0021 model employed in the experiments, showing a chord of 150 mm and a span of 900 mm, coincides with the one used in (Zarketa-astigarraga et al., 2022; Zarketa-Astigarraga et al., 2023). The main difference is that the current study considers the implementation of *PD*s upon the airfoil; the specific geometrical distribution chosen for the analysis is shown in the zoomed portion standing at the bottom of Figure 2b. The employed *PD*s consist of triangularly-shaped stripes with a side length (l) of 13 mm and a height (h) of 1 mm. The distance between adjacent elements (s) is set equal to the side length of the stripes, i.e. $s = l$. The only variable parameter is the dimensionless chordwise distance between the leading-edge of the airfoil and the parallel line at which the *PD*s are placed, namely x/c.

When choosing the elements, the easiness of implementation and removal of *PD*s has been the main criterion to consider. Besides, the triangular shape finds a justification on recent studies that employ similarly-shaped vortex generators for enhancing the aerodynamic behaviour of certain devices, especially in the field of heat transfer and as a means for delaying stall and promoting an attached boundary-layer in a larger portion of the surface (Caliskan et al.; Aksoy; Srivastava and Sahoo). Lastly, the dimensions and parameters of the specific distribution chosen for the study have been determined heuristically. The chosen distribution shows the feature of affecting the development of the boundary-layer in the two configurations tested, to such an extent that it induces noticeable changes in the lift and drag curves.

The experimental protocols also comply with those employed in (Zarketa-astigarraga et al., 2022; Zarketa-Astigarraga et al., 2023); for the sake of conciseness, a brief description is solely provided herein, but further information can be found in (Zarketa-astigarraga et al., 2022; Zarketa-Astigarraga et al., 2023). The flow conditions are determined by the chord-based Reynolds number of the airfoil, measuring the inlet velocity with a *Delta-Ohm HD49047T01L* Pitot-static probe and the ambient conditions via a *Delta-Ohm HD2001.1* transmitter. The lift load upon the airfoil is recorded by a *Kistler 9119AA2* piezoelectric balance fixed to a rotary plate that allows changing the angle-of-attack of the model. The aerodynamic drag is determined by the momentum-deficit method (Meseguer-Ruiz and Sanz-Andrés, 2012), traversing an *Aerolab* type wake-rake across the width of the wind tunnel and measuring the dynamic pressure loss caused by the wake by means of a *Scanivalve MPS4264* differential pressure scanner. A LabVIEW (202, a) application is used for monitoring the system, scheduling the measurements that are recorded with *National Instruments* data-acquisition and control modules.

2.1.2 Flow conditions

Flow paradigms other than the *Clean* one shown in Table 1 require reproducing turbulent and roughness effects within the tunnel. Turbulent intensities (I) reaching $\approx 4\%$ are achieved by means of a passive grid installed at the inlet of the test-section, with integral length-scales (ℓ_0) matching the order of magnitude of the chordal dimension of the airfoil, i.e. $\ell_0/c \lesssim 1$ (Zarketa-Astigarraga et al., 2021; Zarketa-Astigarraga). The passive grid set-up reproduces low-intensity turbulent scenarios that, although they do not match the high turbulence levels encountered in urban areas (KC et al., 2021), they serve for showing if transitional configurations are already sensitive to such low levels of turbulence. Unfortunately, the current experimental set-up does not allow for higher turbulence intensity levels without violating the Kolmogorov's universal decay-law, i.e. losing experimental control upon the turbulent scales and intensities (Zarketa-Astigarraga). A P80 type sandgrain paper owning an average grain height of $\approx 100\ \mu$m is used for emulating degradation effects, complying with the 10% chordwise extent coverage provided in (Khalfallah and Koliub, 2007), as shown in Figure 2b.

The tested flow paradigms correspond to two physical scenarios: a *Clean* flow corresponding to default wind tunnel scenarios, and a *Combined* flow including both turbulence and roughness effects, which is reproduced for a $I = 3.8\%$ turbulent intensity case. Experimental tests are undertaken at three different Reynolds numbers within the transitional regime, namely $\mathrm{Re} = [0.8, 1, 1.2] \times 10^5$. Due to the choking effect of the passive grid, the tunnel is not able to achieve larger Reynolds numbers when the grid is installed (Zarketa-Astigarraga et al., 2021). The measurements performed at each of the case-studies yield the characteristic $c_l - \alpha$ and $c_d - \alpha$. The angles-of-attack cover the range $\alpha \in [0, 20]^{\circ}$, with an angular interval between measurements of $\Delta\alpha = 1^{\circ}$. The multi-parametrical set of variables for the overall experimental campaign is synthesized in Table 1. The "*Bare*" denomination shown in the column for the elements' chordwise position refers to the configurations without *PD*s. These, in the cases they are implemented, are positioned at a quarter of the chord ($x/c = 0.25$, named "*PD25*") and at the mid-chord ($x/c = 0.5$, dubbed "*PD50*"); their graphical definitions are also provided in Figure 2b.

Table 1. parametrical schedule for the experimental testing campaign.

Flow paradigm	**Reynolds number**	**Angular config.**	**Elements' chordwise position, x/c**	**# cases**
Clean	$\text{Re} \in [0.8, 1, 1.2] \cdot 10^5$	$\alpha \in [0, 20]^{\circ}$, $\Delta\alpha = 1^{\circ}$	*Bare*, 0.25, 0.5	9
Combined				9
				Total 18

2.1.3 Uncertainty analysis

Experimental repeatability is ensured by carrying out a threefold set of measurements per case-study, with the datasets in Section 4 providing average values of the three trials. An uncertainty analysis based on (Zarketa-Astigarraga et al., 2020a, b) is performed upon the datasets, with the computed uncertainty intervals corresponding to a 95% confidence level. The maximum, mean and standard deviation values of the c_l and c_d uncertainty intervals are given in Table 2.

Table 2. maximum, mean and standard deviations of the experimental errors.

Flow paradigm	**c_l−related**			**c_d−related**		
	$\delta_{c_{l_{\text{max.}}}}$	$\overline{\delta_{c_l}}$	$\sigma_{\delta_{c_l}}$	$\delta_{c_{d_{\text{max.}}}}$	$\overline{\delta_{c_d}}$	$\sigma_{\delta_{c_d}}$
Clean	4.5×10^{-2}	4.7×10^{-2}	6.8×10^{-4}	1.4×10^{-2}	6.8×10^{-3}	4.1×10^{-3}
Combined	4.7×10^{-2}	4.6×10^{-2}	7.6×10^{-4}	3.5×10^{-2}	1.5×10^{-3}	8.5×10^{-3}

2.2 Numerical set-up

The estimation of AEP (Annual Energy Production) losses is achieved through the numerical implementation of the BEM theory (Glauert, 1935; Manwell et al., 2011), using the open-source QBlade code (202, b). The process follows the same three-step procedure as in (Zarketa-Astigarraga et al., 2023), which is briefly described below and schematised, for illustrative 305 purposes, in Figure 3:

- Users define the airfoil objects for the wind turbine blades, specifying geometrical properties and supplying the polars ($c_l - c_d$ curves) obtained from wind-tunnel experiment data.
- The polars are extrapolated to cover the full 360° angular range using the Viterna extrapolation approach (Viterna and Corrigan, 1982).
- A blade design is configured, and the aerodynamic behavior is simulated using the BEM theory, enabling the calculation of rotor performance over various wind speeds.
- The AEP estimation is performed by adopting a Weibull distribution (Waloddi Weibull, 1951) to model the statistical occurrence rates of different wind speeds, widely used in the wind community for this purpose (Tuller and Brett, 1983). This approach allows a first approximation to the evaluation of AEP losses and the optimization of wind turbine performance.

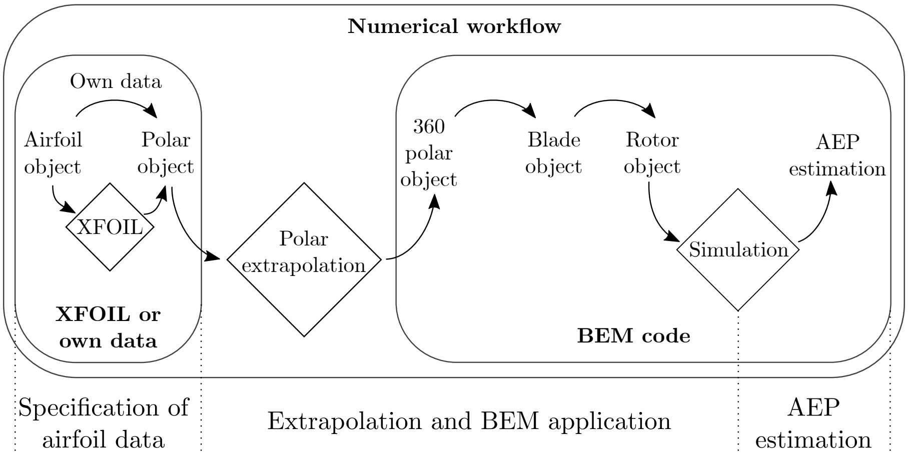

Figure 3. Schematic of the numerical worfklow philosophy followed by QBlade; adapted from (202, b).

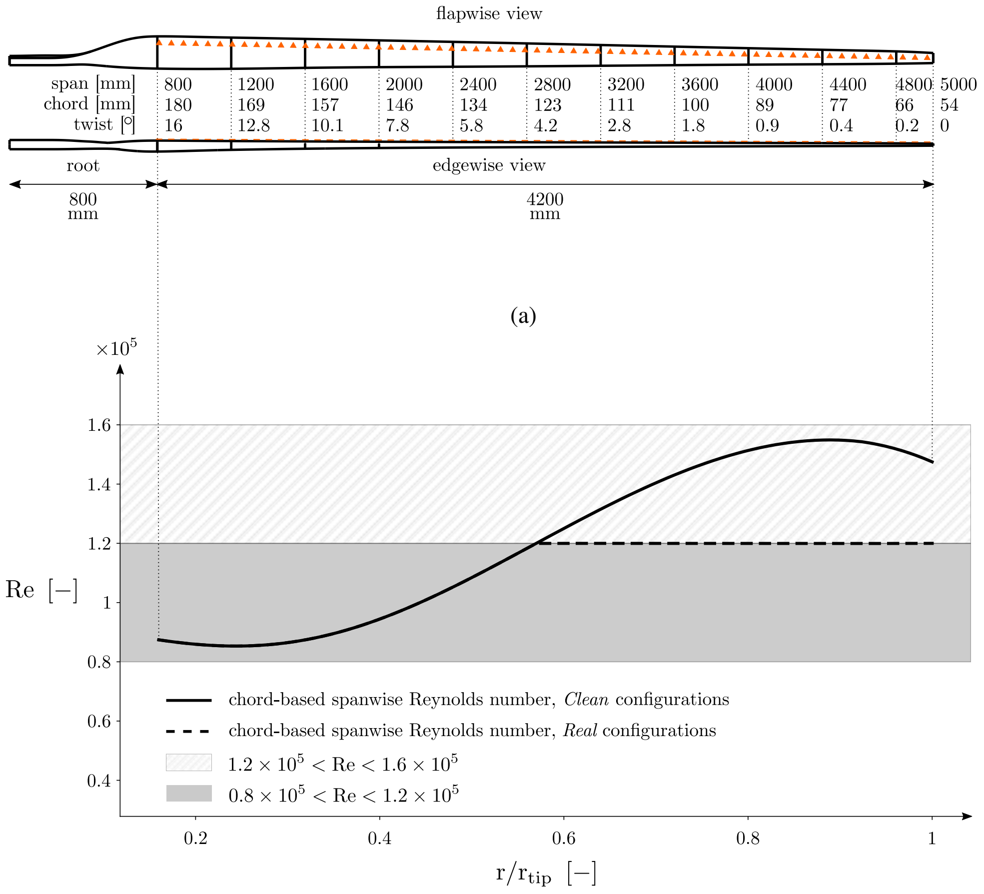

(a)

(b)

Figure 4. Blade-related parameters; (a) chosen blade design equipped with *PD*s; (b) spanwise-varying chord-based Reynolds number.

3 Case-study

3.1 Turbine selection

The workflow discussed in Section 2.2 emphasises the importance of airfoil geometry and turbine blade shape in conducting AEP calculations. Following a previous research by the authors centered on analysing the effect of different flow-paradigms in the AEP of a SHAWT (Zarketa-Astigarraga et al., 2023), the case study developed herein consists on the same 3-bladed turbine inspired by Habali and Saleh's design procedure (Habali and Saleh, 2000), which includes a linearly decreasing spanwise chord variation and a nearly-parabolic twist trend with specific twist values maintained. The flapwise and edgewise shapes of the blade, equipped in the spanwise direction with the *PD*s mentioned in Section 2.1.1, are shown in Figure 4a. Besides, Figure 4b shows the spanwise-varying chord-based Reynolds number at each blade section under *Clean* conditions.

The turbine features a 5-meter-radius rotor, a rated wind speed of 11 m/s, a rotational velocity of 75 rpm, and a design tip-speed ratio (λ) of 3.8, resulting in a rated power of 7.8 kW. It operates under a stall-regulated control mechanism, achieving an average AEP of 30 MWh under *Clean*-flow conditions.

Additionally, the turbine is simulated under a pitch-regulated mechanism, actively adjusting the blade pitch angle at high wind speeds to maintain a constant output power beyond a predefined wind speed value. The QBlade code allows specifying the operational point at which the pitch regulation mechanism comes into play (202, b). Once such a point is reached, the code begins to modify the pitching angle of the blades so that the rotor maintains a constant power output. In the current simulations, the mechanism is set-up individually for each of the flow configurations tested, so that it enters into operation at the peaks of the corresponding power curves. A synthesis of the geometrical and operational turbine parameters may be found in the upper block of Table 3.

3.2 Simulation parameters

The polars of the airfoil objects shown in the workflow of Figure 3 are provided after having established their geometrical specifications. The blade is discretized into $N = 100$ equispaced elements, thus accounting for the Reynolds dependency of the polars. The highlighted areas in Figure 4b correspond to regions for which different experimental datasets are available for the NACA0021 airfoil. The shaded region, i.e. $0.8 \times 10^5 < \mathrm{Re} < 1.2 \times 10^5$, stands for the range for which experimental polars are available at *Clean* and *Combined* flow-paradigms; besides, the hatched area that covers the range $1.2 \times 10^5 < \mathrm{Re} < 1.6 \times 10^5$ refers to the interval for which *Clean*-flow data is only available (Zarketa-astigarraga et al., 2022).

The procedure for obtaining polars at Reynolds values other than the testing ones is borrowed from the previous study by the authors (Zarketa-Astigarraga et al., 2023); an interpolation scheme is employed for computing the $c_l - c_d$ relations at Reynolds numbers falling between the experimental range. The polars of the outer half of the blade sections are considered equal to the curves obtained at $\mathrm{Re} = 1.2 \times 10^5$, as represented by the straight dashed line that parts from the mid spanwise dimension in Figure 4b.

Thus, 33 case-studies are addressed for the analysis of AEP estimations: both the *Clean* and the *Turbulent* paradigms comprise three cases each, corresponding to the *Bare* and the two *PD*-equipped configurations. The *Combined* cases comprise roughness coverage areas spanning the interval $[10, 100]\,\%$, also with the *Bare* and the *PD* configurations.

The shape (k) and scale (A) parameters of the Weibull distribution are set to $k = 2$ and $A = 8.13$ m/s, in accordance with the values employed in (Zarketa-Astigarraga et al., 2023) and whose orders of magnitude comply with the ones in SHAWT applications (Sunderland et al., 2013; Pagnini et al., 2015). Such values provide the nominal AEP of 30 MWh for the *Clean* blade configuration. The two bottom blocks in Table 3 summarise the simulation-related parameters of the computed case-studies.

https://doi.org/10.5194/wes-2025-36
Preprint. Discussion started: 8 April 2025

Table 3. Numerical parameters for the QBlade-simulated rotor.

Rotor-related parameters	
Rotor design	Habali & Saleh. (Habali and Saleh, 2000) inspired
Rotor blades	3
Blade length	5000 mm
Blade geometry	NACA0021
Blade chord	Linear root-tip variation: from 160 mm to 54 mm
Blade twist	Nearly parabolic root-tip variation: from 16° to untwisted
Cut-in speed	2.5 m/s
Cut-off speed	15 m/s
Nominal speed	11 m/s
Nominal rotational speed	75 rpm
Nominal λ	3.8
Nominal power	7.8 kW
Nominal AEP	30 MWh
Regulation	stall-regulated (*SR*) pitch-regulated (*PR*)
Simulation-related parameters	
# blade elements	100
Polar spec.	Experimental
Weibull parameters	$k = 2$ $A = 8.13$ m/s
Case-studies	
Flow-paradigm	**Affected coverage (from tip to root)**
Clean (*Bare*, *PD25*, *PD50*)	0%
Turbulent (*Bare*, *PD25*, *PD50*)	0%
Combined (*Bare*, *PD25*, *PD50*)	$\in [10, 100]\,\%,\ \Delta = 10\%$

355 4 Results and discussion

The results that follow are grouped in two main sections: Section 4.1 is devoted to the aerodynamic analysis of the airfoil under the different flow paradigms and *PD* distributions, emphasising the behavioural changes shown by the model. Such an analysis is extrapolated to a set of typical SHAWTs in Section 4.2.1, with the aim of predicting the impact of a *PD*-based flow-control technique on the AEP loss reduction by means of the QBlade open-source code.

4.1 Aerodynamic behaviour analysis

Figures 5, 7 and 9 show the overall set of tested cases, both for *Clean* and *Combined* flow paradigms, in an increasing order of the tested Reynolds numbers; while Figures 6, 8 and 10 intend to provide a more detailed comparison between the distinct *Combined* configurations, and they are also ordered with respect to increasing Reynolds numbers. Thus, Figures 5a, 6a, 7a, 8a, 9a and 10a show the $c_l-\alpha$ curves obtained at each Reynolds number. In contrast, Figures 5b, 6b, 7b, 8b, 9b and 10b address the $E-\alpha$ curves, where $E=c_l/c_d$ stands for the aerodynamic efficiency of the airfoil.

Given the sensible scale-effect that transitionally-operating airfoils show, the description of the main aerodynamic features is performed following an increasing order of the tested Reynolds number.

4.1.1 Re $= 0.8 \times 10^5$ cases:

- $c_l-\alpha$ **curves:** Figure 5a shows that *Clean* configurations own short-ranged linear regions, with non-linear effects ensuing at angles-of-attack beyond 3°. The linear ranges of the *Combined* configurations extend a wider α interval, reaching saturation without undergoing non-linear effects, but own a much lower linear slope instead. The non-linear tendency of the curves at low angles-of-attack has been ascribed to the formation and presence of laminar separation bubbles (LSBs) in the boundary-layer (Hansen et al.). The effect of a LSB is to induce an apparent cambering of the airfoil. Its shape modifies the path of the streamlines when surrounding the airfoil and, as a consequence, the flow encounters an effective geometry that differs from the theoretical shape of the airfoil. As the LSB structure is highly sensitive to freestream conditions, especially to the Reynolds number and the angle-of-attack, each flow configuration at low α values will correspond to different bubble extents being formed upon the suction-side of the airfoil. Accordingly, the theoretical slope of the $c_l-\alpha$ curve will be affected differently at each angle-of-attack, which results in the observed non-linear behaviour of the airfoil. A more in-depth analysis of the phenomenon can be found in (Zarketa-astigarraga et al., 2022).

  When considering the influence of the flow-control elements, the main difference between the *Bare* and *PD* cases is that the latter induce element-distribution-dependent c_l offsets that are detectable at $\alpha = 0°$. Indeed, the *PD25* cases show negative-valued offsets, causing the initial range of the curve to lie below the *Bare* counterpart, whereas the *PD50* cases show positive-valued deviations. Those offsets occur regardless of the analysed flow-paradigm and Reynolds number, being equally reproduced in Figures 7 and 9. The physical reasoning behind such offsets is that the implementation of the *PD*s upon a single side of the airfoil breaks the inherent symmetry of the NACA0021 model, which ceases to show a null lift value at 0°. However, no plausible mechanism has been found for explaining the different-valued offsets caused by the two distributions.

  Otherwise, the relatively milder offsets caused by the *Combined* configurations are ascribed to the effect of turbulence, which is known to produce an homogenization of the features observed under *Clean* conditions (Zarketa-Astigarraga et al., 2023), a better-appreciated effect in Figure 6a. Such an homogenization is ascribed to the sweeping of the LSBs from the suction-side, which results in the suppression of the non-linear behaviour observed for the *Clean* paradigm. Besides, a relevant difference between the *Clean* and *Combined* configurations is in the preservation of the initial offsets induced by the *PD*s. Such offsets are lost during the non-linear evolution of the *Clean* configurations, with the three curves reaching saturation at the same c_l values. However, it seems that they are better preserved by the *Combined* configurations, mainly due to the promoted linear tendency they show. It is to notice that the linear slopes of the *Combined* flow-paradigm cases lie below the theoretical value, mainly due to the effect that the roughness band induces in the development of the boundary-layer (Zarketa-astigarraga et al., 2022).

The dependence of the offset evolutions with respect to the flow-paradigm links their effect to the LSB structures. It seems that the *PD*s affect the formation of the bubbles noticeably, given that their influence is more apparent in the *Clean* configurations. The *PD25* case, in particular, induces a stronger non-linear trend, which may be interpreted as the flow-control elements amplifying the effect of the bubbles. In contrast, the *PD50* configuration runs in parallel to the *Bare* case, which may indicate that the elements are not capable of influencing the boundary-layer when placed at the mid-section of the chord. As observed in (Zarketa-astigarraga et al., 2022), the boundary-layer has already transitioned into a turbulent regime by then.

Finally, The changes that the *PD*s induce on the saturation and stalling regions of the curves are also flow-paradigm dependent. Whereas the elements may induce either a stall delay (*PD25*) or promotion (*PD50*) in *Clean* configurations, the *Combined* ones do not show noticeable differences on this respect. Once again, the lack of sensitivity of the *Combined* configurations may be explained in terms of the turbulent nature of the boundary-layer developed upon them. The flow-control elements do not show the capability of impacting the development of such a boundary-layer as strongly as they do in the *Clean* flow-paradigm. The post-stalling regions have no remarkable features, mainly because the effects of the *PD*s cease after reaching stall.

- $E-\alpha$ **curves:** Figure 5b shows that the c_l offsets are partially reproduced on the $E-\alpha$ curves, at least for the *Clean* configurations. Indeed, the *PD50* case provides a range of low angular configurations showing marginally improved efficiencies with respect to the *Bare* case. A potential explanation for this observation may stem from a possible vortex-generator-like behavior of the elements at that particular configuration. It seems that they perturb the boundary-layer in a sense that, although not suppressing the LSB structures (as indicated by the non-linear behavior of the $c_l-\alpha$ curve), they achieve to induce a milder development of the turbulent boundary-layer downstream. This would result in a lower drag coefficient, leading to the observed increase in efficiency. Within the saturation region, the *PD50* case falls below its partner curves, showing the poorest behaviour in terms of efficiency. Instead, the *PD25* configuration achieves a range of improved E values, mainly due to a decrease in drag for those angles-of-attack. Besides, the stall delay it induces is translated into an extent of the efficiency curve that performs better than the *Bare* case. Thus, the *PD25* configuration complies with the original purpose of the vortex generators, extending the range of unstalled conditions towards larger angles-of-attack.

The *Combined* case-studies lie noticeably lower than their *Clean* counterparts, showing the negative synergistic effects between turbulence and roughness mentioned in (Zarketa-Astigarraga et al., 2023). The milder slopes they show in the $c_l - \alpha$ curves, coupled with their larger drag coefficients due to the development of the turbulent boundary-layer, makes the *Combined* $E - \alpha$ evolutions show a reduction of more than 33% with respect to the *Clean* characteristics. This essential difference between the efficiency curves of the two flow-paradigms shows that the development a turbulent boundary-layer, although beneficial from the standpoints of bubble suppression or stall delay, may have detrimental effects due to the increased drag coefficients.

Thus, the green-shaded areas in Figure 5b correspond to flow configurations at which any of the *PD* distributions provide an enhancement on the aerodynamic behaviour under *Clean* flow conditions. Besides, it is observed that the overall trend of the *Combined* configurations is to extend the angular range at which the airfoil avoids stall. A better appreciation of the differences among the $E - \alpha$ curves of *Combined* configurations is observed in Figure 6b. The *PD50* case does not improve the behaviour at low α values as in the *Clean* configurations, but it achieves a range of improved efficiencies within $\alpha \in [9, 13]$. Instead, the *PD25* case yields a largely reduced efficiency curve until near-stalling conditions, beyond which it provides a stall-delay-induced efficiency gain that surpasses the other configurations.

4.1.2 Re $= 1 \times 10^5$ cases:

- $c_l - \alpha$ **curves:** the curves shown in Figure 7a indicate that their trends are similar to those observed in Figure 5a, namely: the negative- and positive-valued offsets are reproduced for both the *Clean* and *Combined* paradigms, even with the shorter deviations for the latter, as well as the non-linear tendencies of the *Clean* configurations and the straightened and lower-valued slopes of the *Combined* ones.

  However, increasing the Reynolds number causes a number of changes on the features observed for the Re $= 0.8 \times 10^5$ case. First of all, the non-linear trends ensue for sensibly higher angles-of-attack than for the lowest Reynolds number case. This may be ascribed to the thinner boundary-layer that is developed at larger Reynolds numbers. At low angles-of-attack, the decrease of the boundary-layer thickness causes the formation of smaller bubbles that, additionally, undergo transition faster. Consequently, the curves are liable to follow the theoretical trend for such configurations. The LSBs come into play at larger angles-of-attack, in which the curvature imposed by the airfoil induces higher deviations of the flow from the surface and, thus, appreciable bubble structures that cause the non-linearity.

  Second of all, the increase of the Reynolds number seems to have suppressed the saturation and stalling variations observed among the *Clean* $c_l - \alpha$ curves, with the three cases showing similar saturated c_l trends and equal stalling angles. This phenomenon has also been observed in previous analyses by the authors, and ascribed to the homogenizing effect that the earlier development of a turbulent boundary-layer induces at higher Reynolds numbers (Zarketa-astigarraga et al., 2022).

  Instead, the *Combined PD50* case achieves a non-negligible lift enhancement marked by the green-shaded area in Figure 8a, which constitutes a feature that is not observed at the lower Reynolds number case. The only explanation possible is that the *PD* elements are inducing a perturbation effective enough so that the laminar nature of the boundary-layer is preserved for a larger chordal extent at such angular configurations, just as vortex-generators would do. The *PD25* case remains as the poorest one in terms of the lift outcome, which highlights the strong dependency of the flow-control technique upon the operational conditions.

- $E-\alpha$ **curves:** when considering the $E-\alpha$ curves, Figure 7b shows that the marginal lift improvement of the *Clean PD50* case is kept. However, both the *PD25* and *PD50* lie below their *Bare* counterpart beyond 6°, limiting the use of the flow-control technique to low α values. This may sound sensible, considering that a thinner boundary-layer is more liable to be affected by flow-control elements. Nevertheless, notice that it is the *PD50* configuration the one enhancing the behavior of the airfoil. Probably, this means that the effect of the elements goes to perturbing the turbulent boundary-layer, once such a layer has reached a thickness comparable to the height of the *PD*s. It seems to be the only explanation behind the enhancing behavior of the *PD50* configuration, in contrast to the absence of any gains obtained by its *PD25* counterpart.

  Besides, the *Combined* configurations continue to fall noticeably below the *Clean* curves, with the additional handicap that the stall-delay-induced gain observed at $\mathrm{Re} = 0.8 \times 10^5$ is partially lost. However, Figure 8b shows that the *PD*s are effective in obtaining certain optimized configurations: the *PD50* case achieves improved efficiencies for the angular range at which it yields enhanced c_l values, and the *PD25* case is capable of sustaining a slight efficiency gain due to stall delay. Again, these findings may be interpreted in terms of the different boundary-layer perturbations induced by each of the *PD* configurations, just as explained for the $\mathrm{Re} = 0.8 \times 10^5$ case.

4.1.3 $\mathbf{Re = 1.2 \times 10^5}$ cases:

- $c_l-\alpha$ **curves:** the features of the *Clean* curves do not vary significantly with respect to their lower Reynolds counterparts, as observed in Figure 9a. The relatively thinner boundary-layer induces a sensibly larger extent of linear behavior at low angles-of-attack, and the non-linear effect is restricted to the $\alpha \in [5,9]^\circ$ range, just before saturation begins. The similar saturation tendencies observed for the $\mathrm{Re} = 1 \times 10^5$ case apply equally to this case, although the *PD25* configuration seems to depart sensibly from the parallel trends followed by its counterparts. The relative flattening of its saturation, and the promoted stall behavior it shows, can only be ascribed to the particular effects of the flow-control elements upon the boundary-layer for such a configuration.

  When it comes to the *Combined* flow-paradigm, Figure 10a indicates that the positive-valued offset of the *PD50* case is prematurely lost, with the curve reaching saturation at sensibly lower values than its counterparts and showing, consequently, the poorest lift behaviour. Instead, the *PD25* distribution achieves a sustained lift at high angles-of-attack, improving it beyond the *Bare* case limit.

- $E-\alpha$ **curves:** on the efficiency side, the main conclusion drawn from Figure 9b is that augmenting the Reynolds number produces a decrement on the improvement capabilities of the *PD*s upon the *Clean* configurations. The detrimental effect of reducing the thickness of the boundary-layer is clearly manifested here. The *PD50* case achieves a marginal efficiency enhancement that is lost beyond 5°, and no other positive effects are provided by the implementation of the flow-control elements. The increasing reduction of the boundary-layer that will ensue at larger Reynolds numbers would turn the *PD*s into a technique to be avoided at low angles-of-attack.

The *Combined* flow-paradigm shows an equally detrimental evolution with the Reynolds number, yielding efficiency values that fall above 60% with respect to their *Clean* counterparts, an effect already discussed in (Zarketa-Astigarraga et al., 2023).

However, the *PD25* configuration achieves a substantial efficiency gain at high angles-of-attack as shown in Figure 10b, mainly due to a stall delay phenomenon. It is apparent that the flow-control elements act as vortex generators in such a configuration, and that they are capable of perturbin the boundary-layer in a manner that avoids its premature separation, thus preventing stall. Nevertheless, such a behavior contrasts wit the one obtained by the *PD50* configuration, which shows largely reduced values throughout the tested interval. Once again, the large differences between the *PD25* and *PD50* configurations indicate that the passive flow-control technique is not versatile, in the sense that it will probably show a narrow range of flow configurations in which it proves itself beneficial. Extending such a range would require the capability of modifying the distribution of the *PD* elements depending on the flow configuration, i.e. it would require the implementation of an active flow-control technique.

In order to draw a number of conclusions from the above analysis, Figure 11 shows a comparison of the relevant aerodynamic parameters represented in Figures 5 to 10.

Figure 11a corresponds to the maximum lift coefficient values, at each of the tested Reynolds numbers, for the overall set of configurations. As observed, an increase in the Reynolds number causes the $c_{l_{\max}}$ values of the *Combined* configurations to fall progressively below those of the *Clean* ones. The values depicted above the bars represent the relative differences, in percentage, with respect to the *Clean Bare* case (*Clean* and *Combined* configurations) and the *Combined Bare* case (*Combined* configurations only). Even if the mentioned c_l drop depends on the particular layout of the airfoil, meaning that the differences are distinct for the *Bare* and *PD* cases, the worst-case scenarios show $c_{l_{\max}}$ decrements above 30% when compared to the *Clean* baseline configuration. However, and in spite of observing a straightforward tendency with respect to the Reynolds number, the trend is not as clear when comparing the *Bare* and *PD* configurations. The *PD25* cases induce a slight increment if the *Clean*-flow paradigm is considered at $\mathrm{Re} = 0.8 \times 10^5$, or the combined-flow one at $\mathrm{Re} = 1 \times 10^5$, but is detrimental otherwise. As for the *PD50* case, it provides no lift enhancement within the *Clean*-flow paradigm, but it improves it slightly when considering combined-flow conditions at the highest Reynolds numbers. Despite such behaviours not being conclusive enough for establishing a well-defined effect of the flow-control technique, it does seem that larger Reynolds numbers make the differences between *Bare* and *PD* configurations more acute. This is probably due to the correspondent decrease in the boundary-layer thickness, which makes the configuration more sensible to the geometrical patterns implemented along the airfoil's surface. Were the tests undertaken at larger Reynolds numbers, the relative differences observed between the *Bare* and *PD* cases at the $\mathrm{Re} = 1.2 \times 10^5$ datasets would probably become more evident.

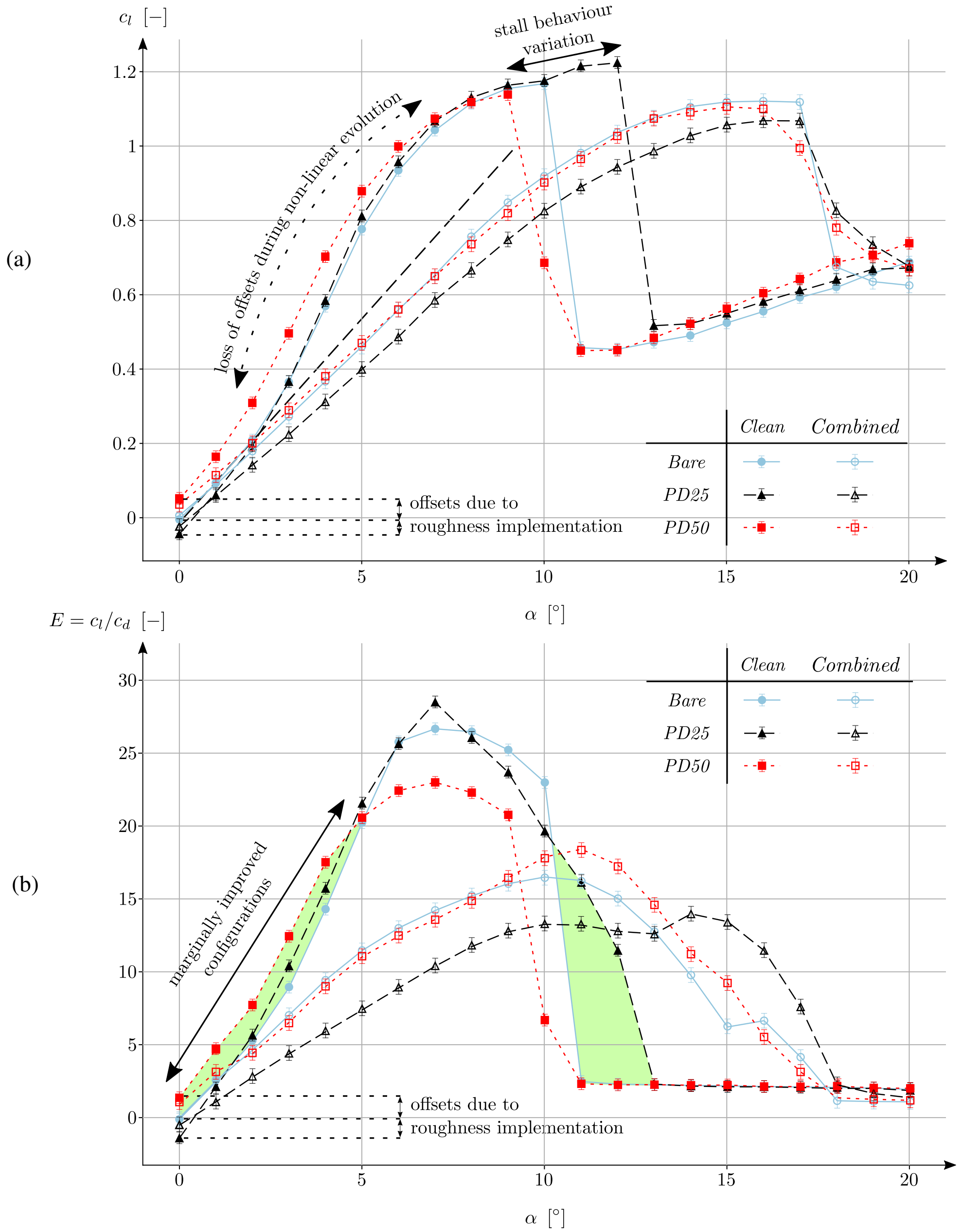

Figure 5. $c_l - \alpha$ (a) and $E - \alpha$ (b) curves for *Clean* and *Combined* flow paradigms with different *PD* configurations at Re=0.8×10^5.

Figure 11b deals with the maximum efficiency values instead. The Reynolds-dependent trend observed when analysing the $c_{l_{\text{max.}}}$ parameter get enhanced, with efficiency drops standing above 40% in the worst-case scenario at $\text{Re} = 0.8 \times 10^5$, and increasing up to 70% for $\text{Re} = 1.2 \times 10^5$. The differences between *Bare* and *PD* cases show a behaviour as inconsistent among Reynolds numbers as in the $c_{l_{\text{max.}}}$ comparative. Within the *Clean*-flow paradigm, the *PD25* case achieves a 16% enhancement

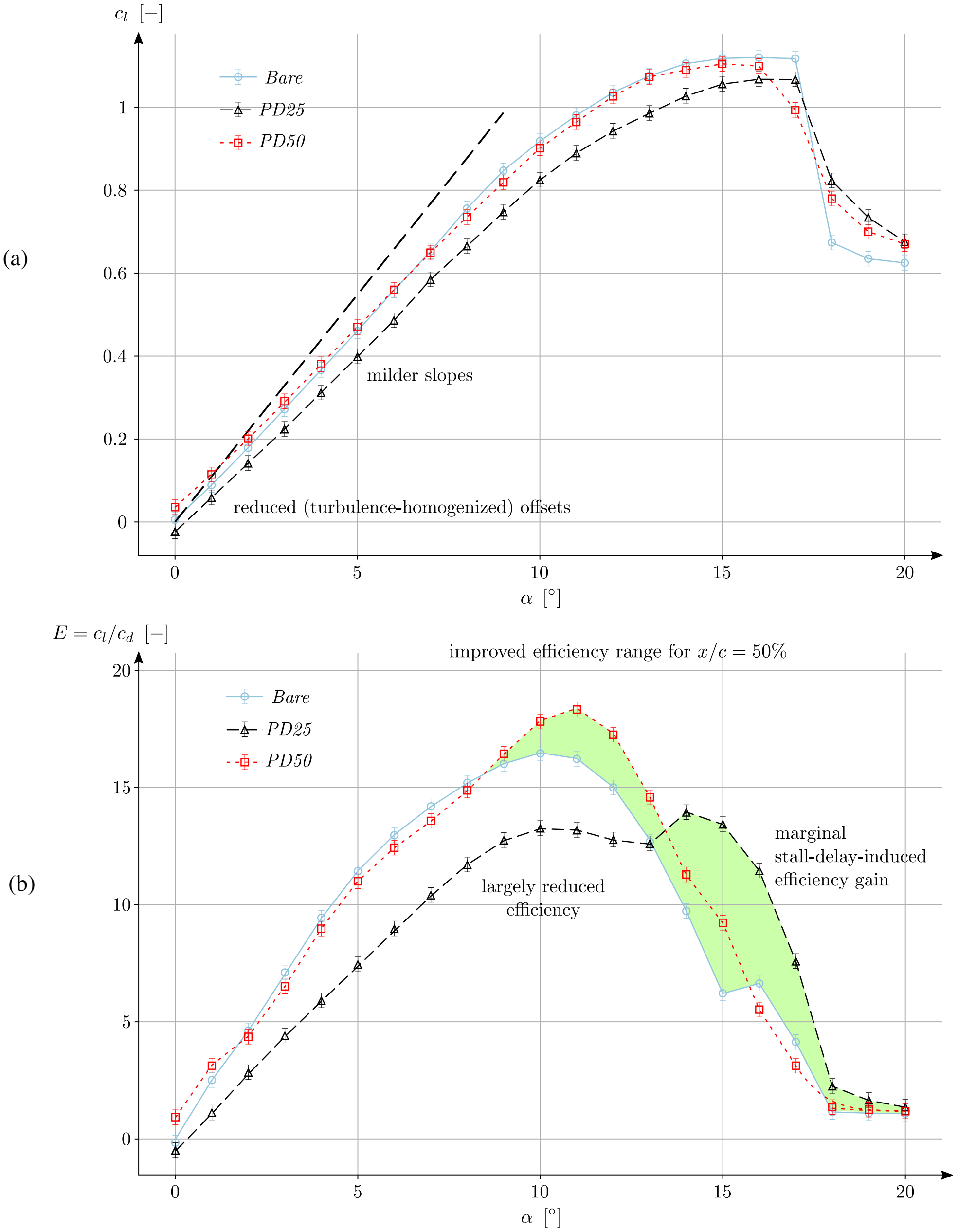

Figure 6. $c_l - \alpha$ (a) and $E - \alpha$ (b) curves under *Combined* flow conditions with different *PD* configurations at Re=0.8×10^5.

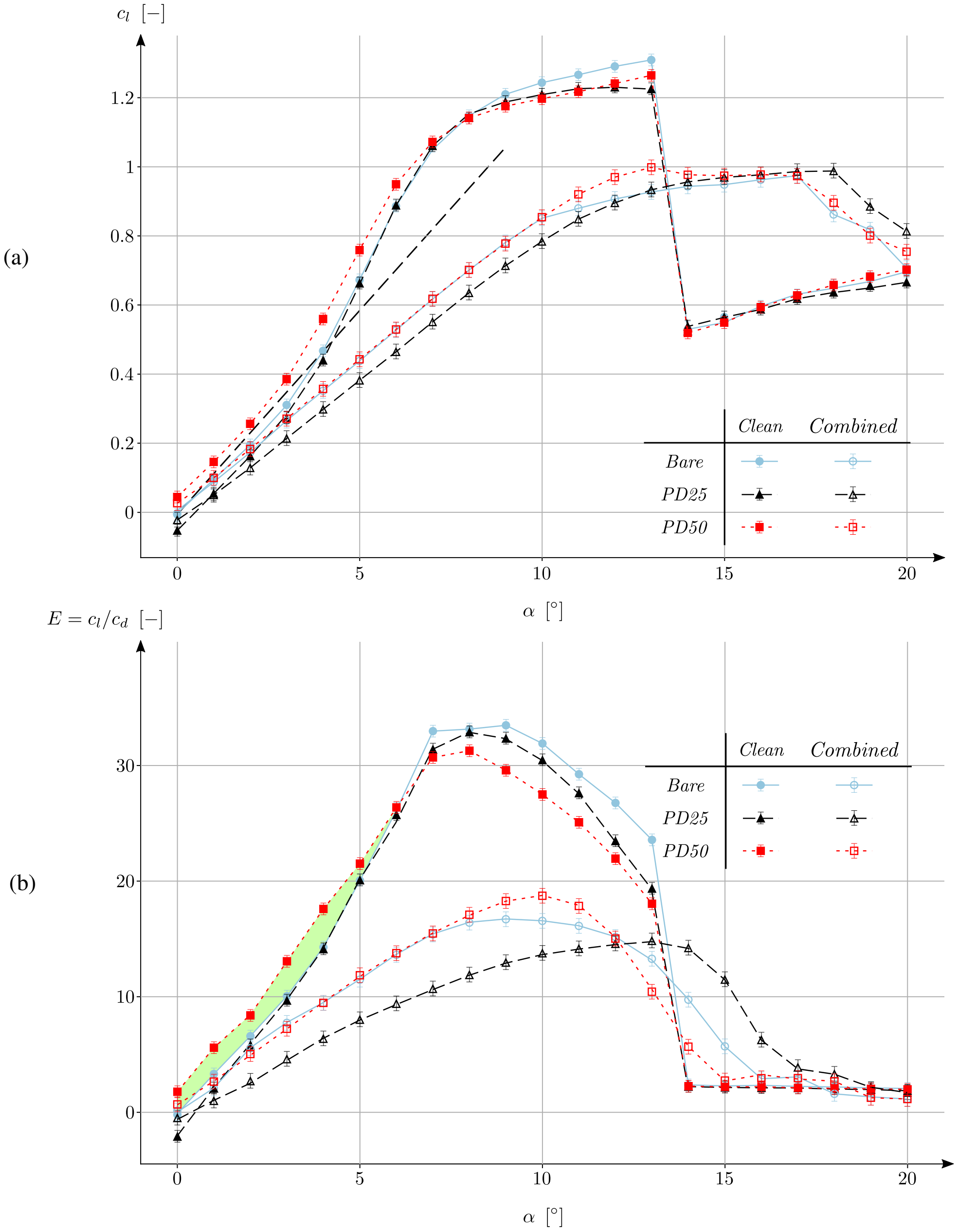

Figure 7. $c_l - \alpha$ (a) and $E - \alpha$ (b) curves for *Clean* and *Combined* flow paradigms with different *PD* configurations at Re=1×10^5.

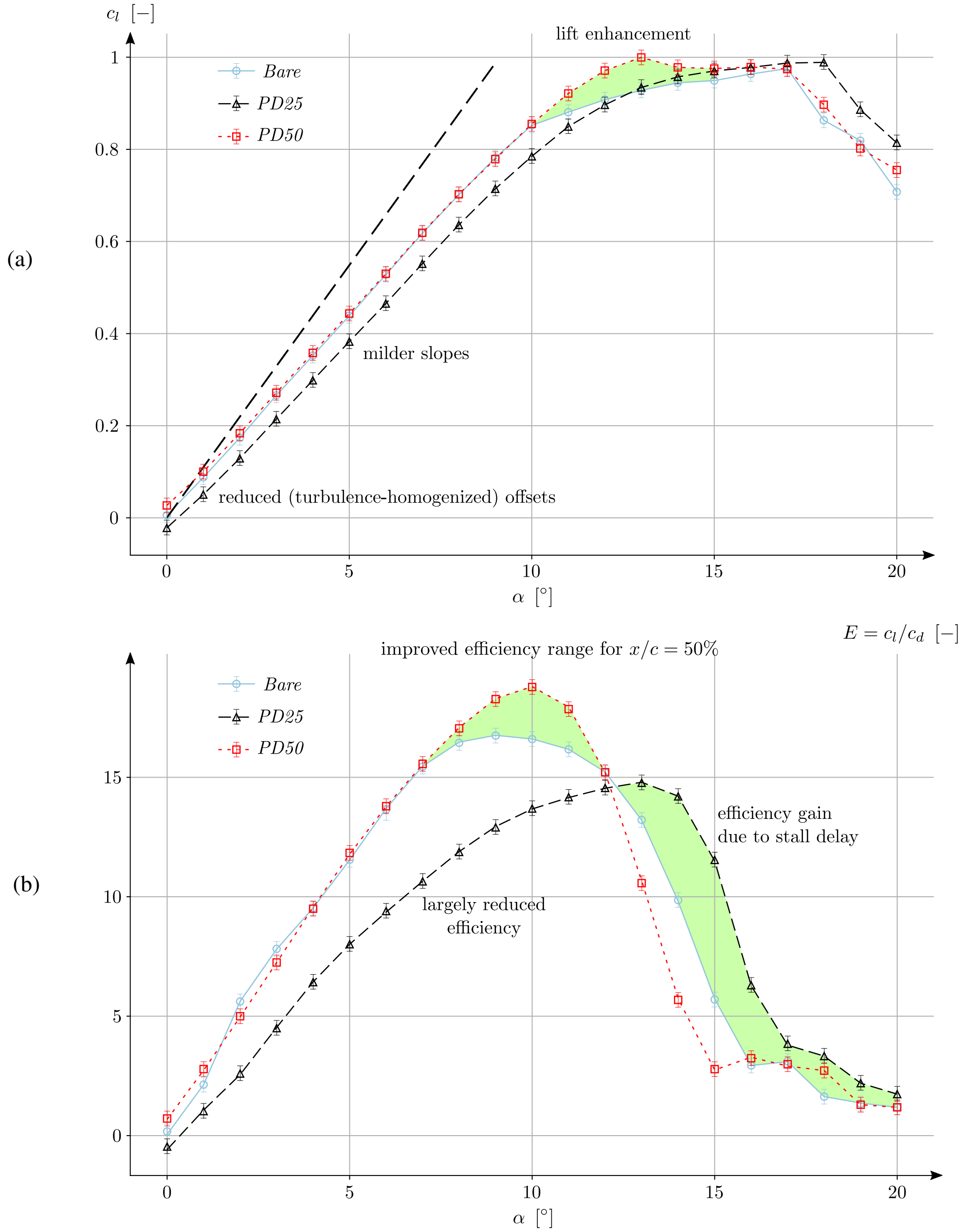

Figure 8. $c_l - \alpha$ (a) and $E - \alpha$ (b) curves under *Combined* flow conditions with different *PD* configurations at Re=1×10^5.

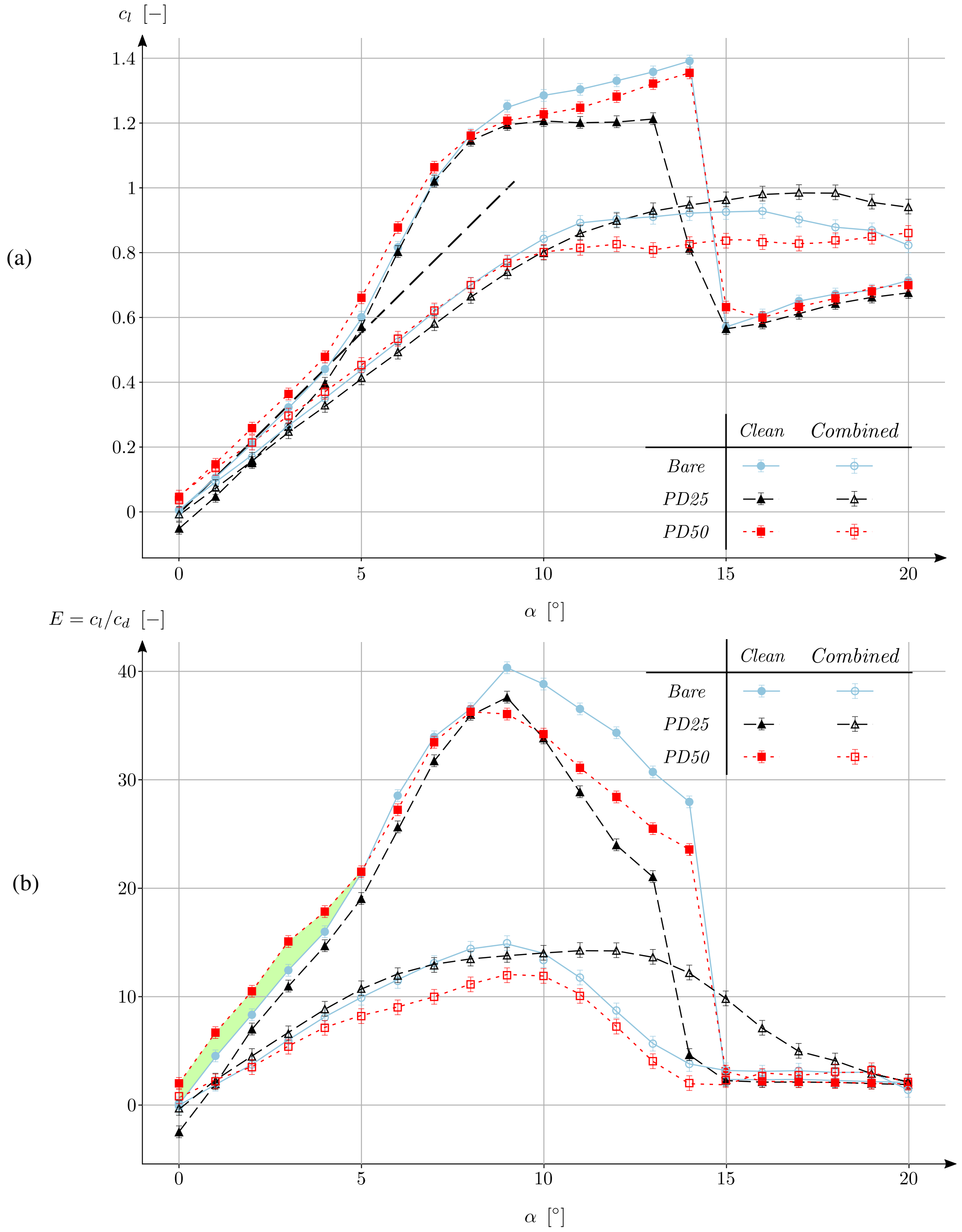

Figure 9. $c_l - \alpha$ (a) and $E - \alpha$ (b) curves for *Clean* and *Combined* flow paradigms with different *PD* configurations at Re=1.2×10^5.

https://doi.org/10.5194/wes-2025-36
Preprint. Discussion started: 8 April 2025

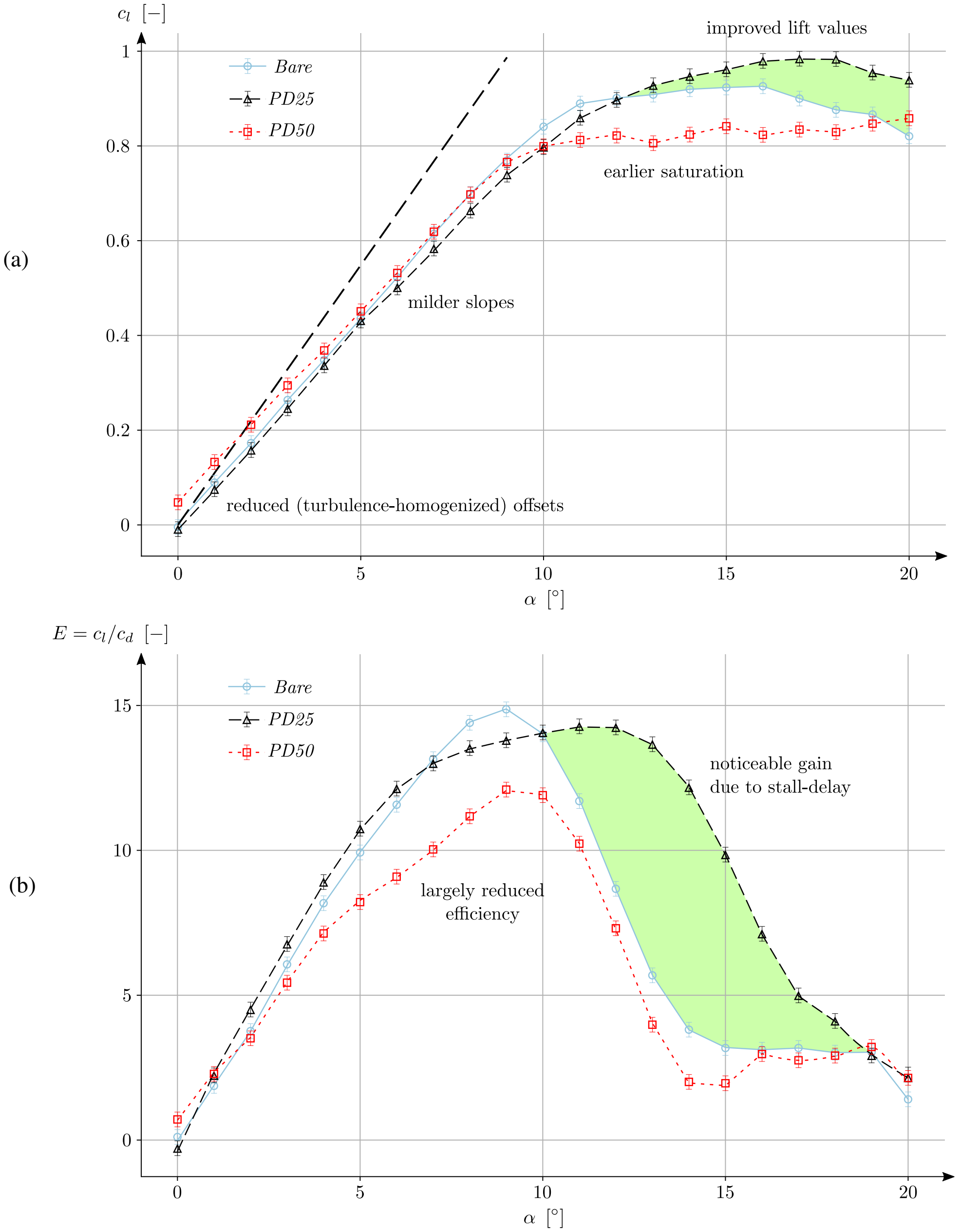

Figure 10. $c_l - \alpha$ (a) and $E - \alpha$ (b) curves under *Combined* flow conditions with different *PD* configurations at Re=1.2×10^5.

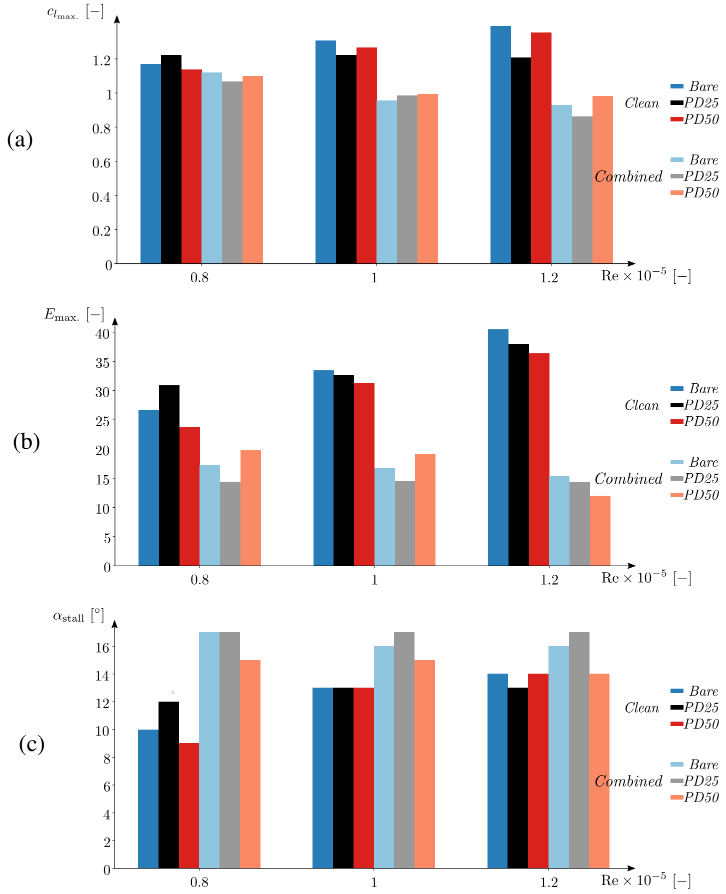

Figure 11. Synthesis of the relevant aerodynamic parameters represented in Figures 5 to 10; (a): $c_{l_{\max.}}$ comparative; (b): $E_{\max.}$ comparative; (c) α_{stall} comparative.

with respect to the *Bare* case at $\mathrm{Re} = 0.8 \times 10^5$, whereas the *PD50* case deteriorates the efficiency by 11%. But those trends change when increasing the Reynolds number, and both *PD* cases produce an efficiency drop at higher wind-speed conditions, with such a drop becoming sensibly larger while augmenting the Reynolds parameter. As for the combined-flow paradigm, the *PD25* case is unable to improve the efficiency with respect to the *Combined Bare* configuration, but the drop it induces is progressively attenuated when increasing the Reynolds number. On the other hand, the *PD50* configuration is capable of enhancing the efficiency well over 10% for the lowest Reynolds number cases, but it becomes the worst-case scenario at $\mathrm{Re} = 1.2 \times 10^5$, showing a drop of 70% with respect to the *Clean* baseline, and a 22% one when compared to the *Combined Bare* case. As occurs with the $c_{l_{\max.}}$ parameter, a trend can be devised for larger Reynolds numbers, with the differences observed within the *Clean* configurations, on the one side, and within the *Combined* ones, on the other, being likely to accentuate with increasing wind-speeds.

https://doi.org/10.5194/wes-2025-36
Preprint. Discussion started: 8 April 2025

Figure 11c represents the comparative chart of the stalling angles, i.e. α_{stall}. The Reynolds-dependent trend observed in $c_{l_{\text{max.}}}$ and $E_{\text{max.}}$ is not present anymore, and the relatively higher stalling angles of the *Combined* configurations stem from the perturbing effect of the turbulent eddies inducing a more robust boundary-layer that sustains a larger pressure drop without detaching from the surface, as explained in (Zarketa-astigarraga et al., 2022). As for the effect of the *PD* elements, different trends are observable: the *PD25 Clean* configuration passes from inducing a stall delay at $\text{Re} = 0.8 \times 10^5$ to causing a slight promotion at $\text{Re} = 1.2 \times 10^5$, whereas the *Combined* configuration is capable of avoiding the promotion of stall at every Reynolds number, even of delaying it minutely. The *PD50* case shows a different evolution: within the *Clean* configurations, it goes from promoting stall at $\text{Re} = 0.8 \times 10^5$ to inducing no changes in the rest of configurations; instead, within the *Combined* configurations the implementation of roughness elements is detrimental regardless of the considered Reynolds case.

As mentioned in Section 1.4, one of the assumptions of the present work is that, concerning the airfoil analysis, it focuses on the evolution of the global aerodynamic parameters, namely the lift and drag coefficients or the stalling angle. Such an analysis is not exhaustive at all, and may prove insufficient for understanding complex phenomena such as the influence of turbulence and roughness on laminar-turbulent transition. A more detailed understanding of such processes would require accounting for the evolution of local parameters, which may be quantified via surface pressure distributions or captured by means of oil-flow visualizations. A first attempt has been carried out by the authors to undertake such an analysis upon the same experimental configuration, and the results have been published for the *Clean* flow-paradigm (Zarketa-astigarraga et al., 2022). Without wishing to diminish the relevance of the global parameters, which constitute the basis of the next section, the application of local measurement techniques to the *Combined* configurations, either with or without *PD* elements, is left as a future research line.

4.2 SHAWT analysis

The basic aerodynamic features described in Section 4.1 have a straightforward translation in terms of both the SHAWT-related power production and the system's structural integrity. In turn, such changes induce a variation in the AEP value, which may be considered as the primary indicator showing the detrimental effect of environmentally perturbing agents and the enhancing potential of *PD* elements. On this respect, the current subsection is divided into two main blocks: Section 4.2.1 discusses the power curves of the SHAWT, and Section 4.2.2 is devoted to showing the effect that the variations of the power curves have in the estimated AEP values.

4.2.1 SHAWT power curves

The three relevant cases, namely *Bare*, *PD25* and *PD50*, are plotted in Figure 12 for different values of the roughness-affected area. Such a coverage is represented by a progressive fading of the plot lines, with a stronger transparency correlating with a higher affected area. Additionally, and as pointed out in Section 3, the turbine has been simulated under stall- (*SR*) and pitch-regulated (*PR*) control mechanisms. The *SR*-related curves are represented by solid lines, whereas the *PR*-ones correspond to the dashed ones.

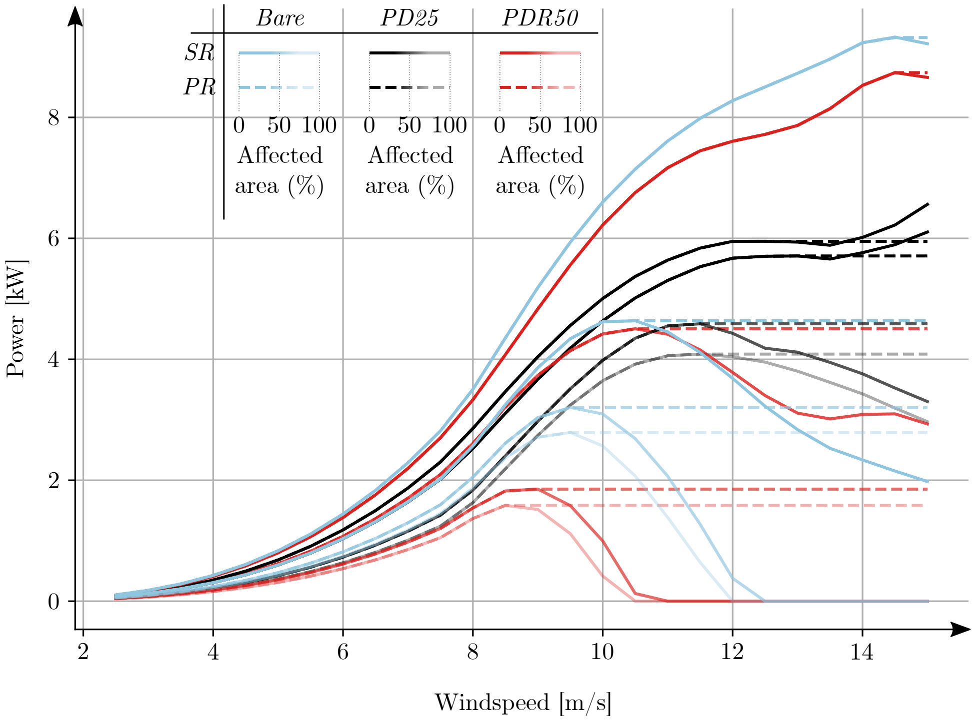

Figure 12. Power curves for the *Bare*, *PD25* and *PD50* cases with different affected areas.

The baseline curve corresponds to the 0% coverage case of the *Bare* configuration. Such a curve refers to the SHAWT operating under turbulent conditions exclusively. Neither environmentally-induced roughness nor *PD*s are present, which emulates the operating conditions of a newly installed turbine. As observed, the power curves corresponding to the rest of the cases lie below the baseline configuration. This is indicative of two relevant aspects: first, that the effect of environmentally-induced roughness is detrimental, regardless of the case considered. Second, that both *PD* configurations also induce a power loss with respect to the baseline. Neither the positive lift offsets nor the efficiency enhancements observed in Figures 5, 7 and 9 seem to play a beneficial role. Instead, it appears that the detrimental effects stemming from the implementation of *PD*s prevail.

Furthermore, such negative effects cause a larger power loss in the case of the *PD25* layout, which lies significantly below the *PD50* configuration. The relative difference between the *PD25* and *PD50* cases may be explained by the positive lift offsets of the latter, already identified when discussing Figures 5, 7 and 9. As mentioned before, the *PD25* curves lie below the baseline configurations throughout the overall angular range, regardless of the considered Reynolds number. Instead, the *PD50* ones achieve a gain, both in c_l and E terms, at low and moderate angles-of-attack. The contributions of such enhanced lift and efficiency values at the linear region of the curves seem to be critical. Indeed, they count for the closeness of the *PD50* case to the baseline, when compared to the *PD25* configuration.

When considering larger affected areas, it is observed hat the three configurations (*Bare*, *PD25* and *PD50*) show a significant deterioration of their power, providing a gradually lower power production. Such a drop depends strongly on the considered case. For the family of curves of representing the *Bare* configurations, the power peak reduces by 50% for a relatively low coverage area (20%); the reduction saturates afterwards, and reaches a minimum of 35% of the baseline's peak value for the full coverage case. As observed, this drop is accompanied by a decrease on the wind speed value for which the maximum power is obtained; such a speed falls from 15 m/s at the baseline to 10 m/s at 100% coverage. These two aspects deteriorate noticeably for the *PD50* configuration, with the power peak dropping below 25% of its nominal value for the 100% coverage, and the wind speed at which such a peak is attained falling as low as 9 m/s. Instead, the *PD25* configuration does not show such a variation; the power peak drops to 66% of its nominal value in the worst-case scenario, with its corresponding wind speed decreasing until 11 m/s.

The aerodynamic differences remarked when discussing Figures 6, 8 and 10 may justify the power curve variations observed above. Those plots show that, when facing *Combined* conditions, the relative gains of the *PD50* configuration obtained under *Clean* flow paradigm lose their relevance and, instead, the *PD25* arrangement begins to show an enhanced behaviour, especially at high angles-of-attack. Thus, the moderate lift gains and the substantial stall delays that lead to significant efficiency increments arise as the main mechanisms behind the sustained power curves shown by the family of curves of the *PD25* case.

One last observation concerns the differences between the *SR* and *PR* curves, when interpreted in terms of the three configurations. It is noteworthy that, for the 0% coverage, both regulation mechanisms play equally well for the *Bare* and *PD50* cases, and that the *PR* mode may even be inducing a power loss for the *PD25* configuration. However, the pitch regulation becomes relevant at larger coverage values, in particular for the two former cases. The larger power drops experienced by the *Bare* and *PD50* configurations make their *SR* curves better candidates for being enhanced when a pitch regulation is implemented. Indeed, the wind speed values at which the power peaks are attained decrease with the coverage area more noticeably for the *Bare* and *PD50* configurations than for the *PD25* arrangement. As such, the pitch regulation mechanism enters earlier for the former cases, which turns it into a proper control strategy at high coverage values for the *Bare* and *PD50* configurations, in particular.

4.2.2 AEP loss estimations

As mentioned in Section 3, the AEP estimations are carried out by considering a Weibull distribution of the wind speeds (Waloddi Weibull, 1951). The estimation itself comes from a convolution operation between the power curves and the Weibull distribution. As such, the AEPs may be interpreted as synthesising each power curve in Figure 12 into a scalar value. Figure 13 gathers the overall set of such AEPs, comprising the *Bare*, *PD25* and *PD50* cases at different coverage areas and for both the *SR* and *PR* modes.

The general trend in Figure 13 is clear: the AEPs decrease as the coverage area increases. Those drops are exponential, showing their steepest variations for the lowest coverage areas and saturating afterwards. The observed exponential trend makes sense insofar the blades are assumed to begin their progressive degradation from the tip inwards. As the tip sections are the ones that contribute the most to the power production, their premature degradation largely affects the final value. In addition, it is to notice that the AEP of the *Bare* case under *Clean* conditions matches the nominal value of 30 MWh which,

https://doi.org/10.5194/wes-2025-36
Preprint. Discussion started: 8 April 2025

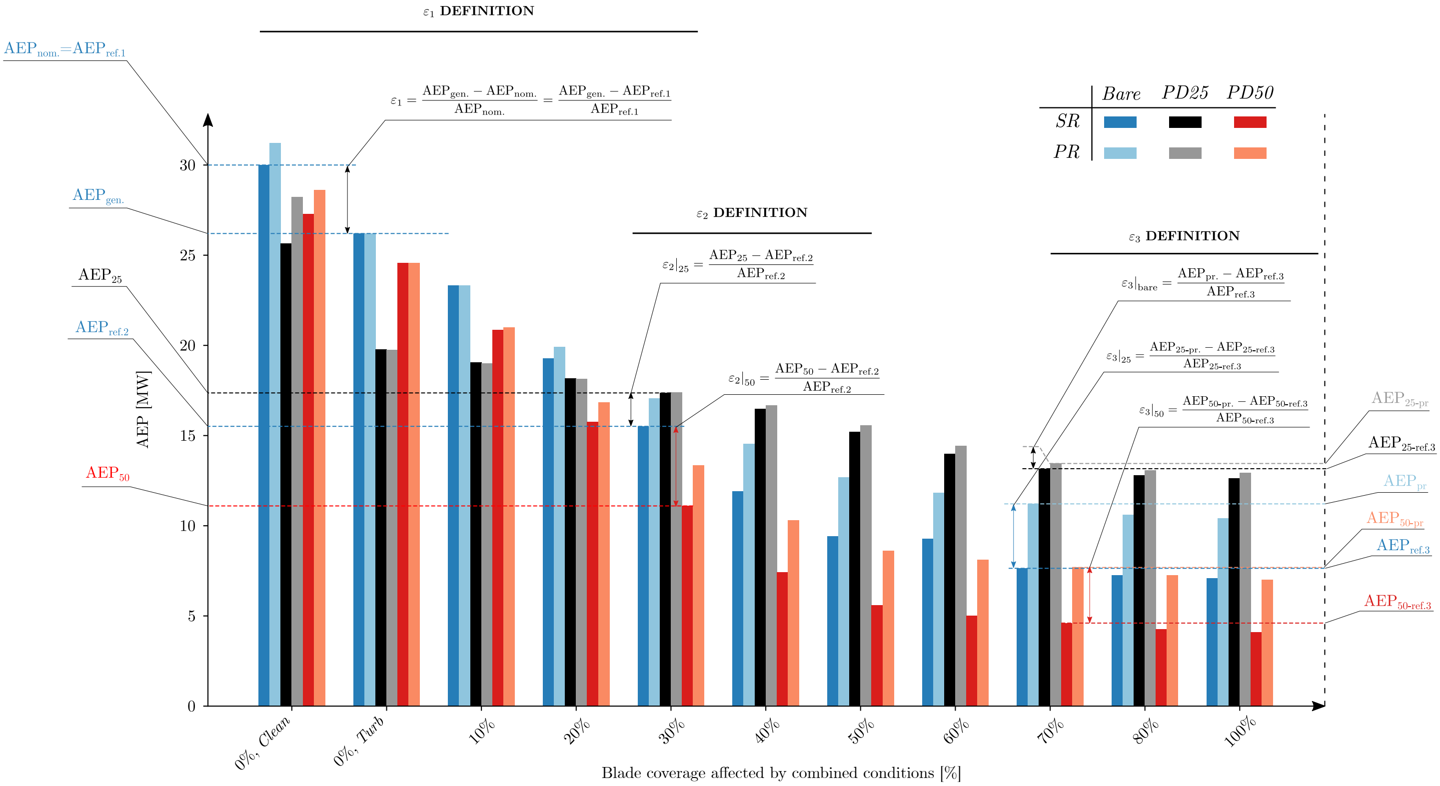

Figure 13. AEP values for the *Bare*, *PD25* and *PD50* cases simulated at different coverage areas and both the stall- and pitch-regulated controls. The graphical definitions of the $(\varepsilon_1, \varepsilon_2, \varepsilon_3)$ loss factors is also provided.

as mentioned in Section 3, constitutes the baseline configuration employed for determining the parameters of the Weibull distribution.

620 Besides the straightforward interpretation that Figure 13 provides, the data on the chart may be broken down so that the contributions of key turbine aspects considered in the study become evident. For such a purpose, three different loss factors are defined, namely $(\varepsilon_1, \varepsilon_2, \varepsilon_3)$. Their graphical definitions are given in the figure itself, and its formal expression reads:

$$\varepsilon_\bullet = \frac{\text{AEP}_{\text{gen.}} - \text{AEP}_\bullet}{\text{AEP}_\bullet} \cdot 100\ [\%], \tag{1}$$

with $\text{AEP}_{\text{gen.}}$ being the AEP value of the generic case being considered, and $\text{AEP}_\bullet$ being the referential value that defines each 625 of the loss factors. Notice that, with the definition above, a negative $\varepsilon_\bullet$ value correlates with an AEP loss of the generic case with respect to the referential case. Instead, a positive value stands for a gain. As for the loss factors themselves:

- ε_1 **loss factor:** it corresponds to the AEP loss that a generic configuration experiences with respect to the nominal case, i.e. $\text{AEP}_\bullet = \text{AEP}_{\text{nom.}} = \text{AEP}_{\text{ref.1}}$. For illustrative purposes, the ε_1 factor is defined for the stall-regulated *Bare* case owning a coverage area of 0% in Figure 13, and its values are depicted on Figure 14. As observed, except for the *PR* mode of the *Bare* configuration at a 0% coverage area, the overall set of cases induces an AEP loss with respect to the nominal case.

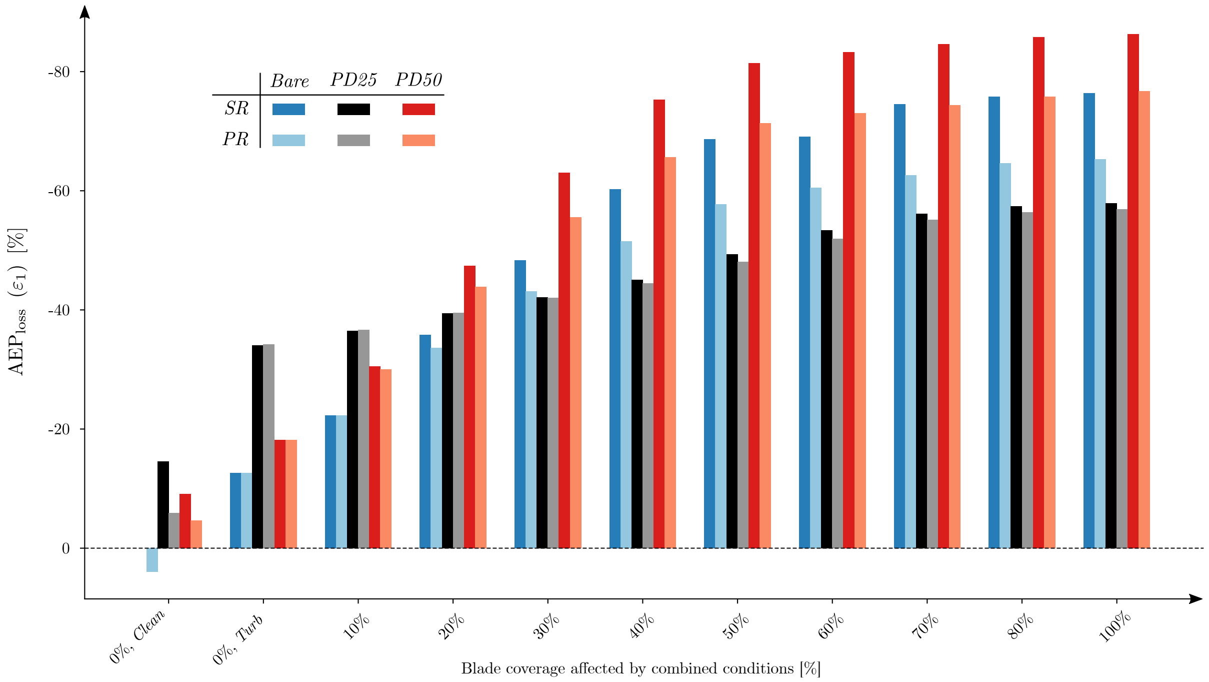

Figure 14. ε_1 loss factor for the *Bare*, *PD25* and *PD50* cases simulated at different coverage areas and both the stall- and pitch-regulated controls.

Figure 14 may be viewed as a horizontal symmetry with respect to Figure 13, as the current $y-$axis represents the AEP loss of each case when compared to the nominal configuration. The higher the coverage area, the larger the loss, reaching values up to -80% for the *PD50* configuration. Such an order of magnitude is not surprising in a SHAWT, considering that the authors have found AEP losses of the sort in a previous study accounting AEP estimations in the same turbine subjected to different flow paradigms (Zarketa-Astigarraga et al., 2023). On this respect, the $\approx -70\%$ AEP losses encountered in the *Bare* configuration, which lie close to the *PD50* values, constitute expected results. The steep AEP losses occurring at low coverage areas and the subsequent saturation at moderate and high ones is clearly represented as well.

Two additional features are remarkable in the chart. The first is that the *PD25* case seems to perform substantially better at high coverage areas than its *PD50* counterpart, although such a behavior does not take place at low coverages. This aspect is to be addressed by the ε_2 factor. The other consideration is that the differences between the *SR* and *PR* cases appear more relevant for the *Bare* and *PD50* cases, especially at high coverage values. It constitutes a feature that the ε_3 takes into account further on.

- ε_2 **loss factor:** it refers to the AEP loss of a stall-regulated case when measured with respect to the stall-regulated *Bare* case owning the same coverage area, which is named as $\text{AEP}_{\bullet} = \text{AEP}_{\text{ref.2}}$. The purpose of ε_2 is to quantify, in relative terms, the effect of implementing *PD*s in a given configuration. Figure 13 shows the graphical definition of ε_2 for the *PD25* and *PD50* cases with a coverage area of 30%. This second loss factor is represented in Figure 15 and, following its definition, merely the comparison of the *SR* controlled *PD* cases with respect to their corresponding *Bare* counterparts are depicted.

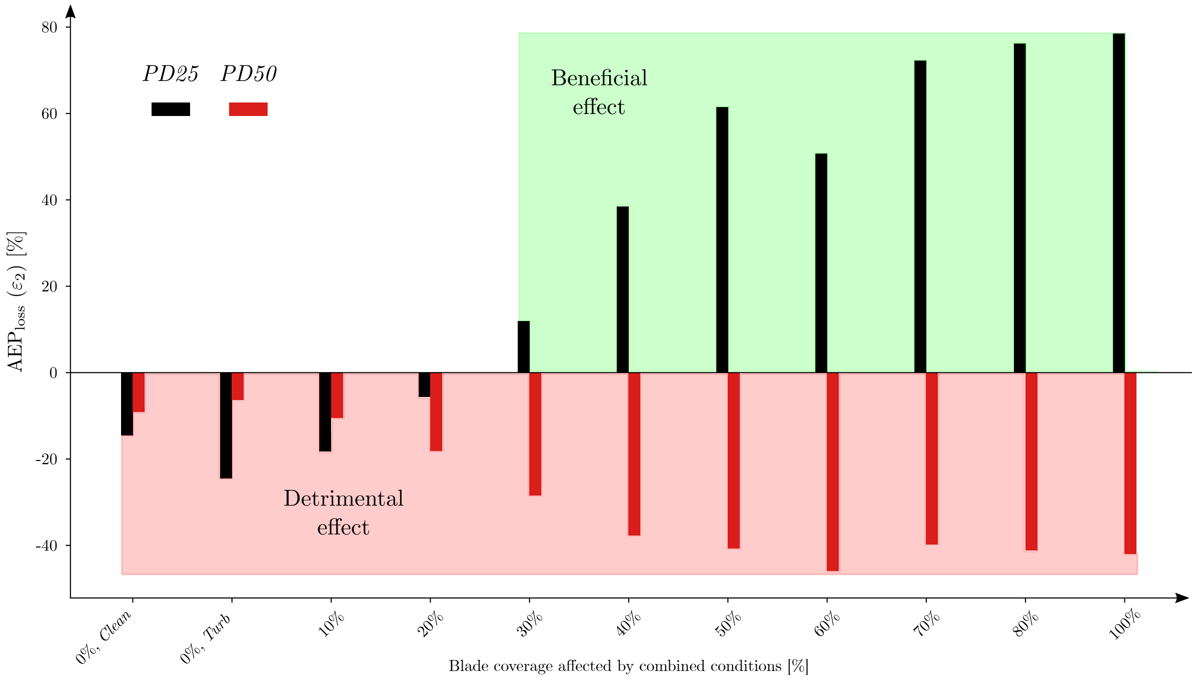

Figure 15. ε_2 loss factor for the *PD25* and *PD50* configurations simulated at different coverage areas.

The chart can be clearly divided into two regions. The upper one, for which the loss factor adopts positive values, implies that ε_2 does not represent a loss as such, but a gain. In other words, the configurations for which $\varepsilon_2 > 0$ perform better than their *Bare* counterparts, showing an enhancement with respect to the baseline case in terms of AEP or, equivalently, a beneficial effect of the *PD*s. The lower region is the reciprocal of the upper one, and implies a detrimental effect of the roughness elements.

As observed, Figure 15 represents a synthesis of the main features discussed in Sections 4.1 and 4.2.1. The first is that the *PD*s do not play a positive role in the case of *Clean* surfaces. Seemingly, implementing such elements may turn beneficial, solely, at coverage areas above 30%. This effect is a straightforward consequence of the enhanced lift and efficiency values of the *PD25* case operating under the *Combined* flow paradigm, achieving to enhance the AEP up to 80% with respect to its *Bare* counterpart at a 100% coverage area.

The second feature to be highlighted is the apparently different effects caused by the *PD25* and *PD50* configurations. Apart from the *PD50* configuration being detrimental regardless of the coverage area, the induced AEP variations are half of those caused by the *PD25* case. This is also due to the lower impact that the *PD*s induce upon the aerodynamic curves when arranged in the *PD50* layout, as discussed in Section 4.1. Besides, it is to mention that the $c_l-\alpha$ and $E-\alpha$ curves, when considered at Re$\in[0.8,1]\times10^5$, are not as detrimental in the *PD50* case as at Re$=1.2\times10^5$. Indeed, the sensible lift and efficiency gains that are observed at moderate angles-of-attack for the lowest Reynolds number cases contrast with the overly deteriorated curves that ensue at Re$=1.2\times10^5$. The upshot is that, according to Figure 4b, the outer half of the blade is subjected to the largest Reynolds number and, accordingly, the *PD25* configuration prevails considerably with respect to the *PD50* one. Therefore, the so-called scale-effect (i.e. Reynolds number dependence) is critical when considering not only the local aerodynamic behavior related to the blade, but the global power production corresponding to the SHAWT system.

- ε_3 **loss factor:** it refers to the AEP loss of a pitch-regulated case when measured with respect to the stall-regulated case owning the same coverage area and the same *PD* layout (either *Bare*, *PD25* or *PD50*), and the corresponding reference is named $\mathrm{AEP}_\bullet=\mathrm{AEP}_{\mathrm{ref.3}}$; ε_3 quantifies the effect of implementing a pitch-regulated control mechanism in the overall AEP. The graphical definition is given for the three configurations owning a coverage area of 70%. This third loss factor is represented in Figure 16. According to its definition, it quantifies the effect of introducing a pitch-regulated control with respect to its stall-regulated counterpart, and it does so for each of the *Bare*, *PD25* and *PD50* cases considered at the set of different coverage areas.

  In a sense, ε_3 may be understood as complementing ε_2, as it provides information on how much the AEP loss is mitigated by the implementation of a pitch regulation mechanism. Indeed, the negative values observed for the *PD25* configuration for coverage areas ranging between $0-30\%$ are negligible, and the overall set of values in the chart may be considered either null (not contributing to a variation when passing from *SR* to *PR*) or positive (inducing not an AEP loss, but a gain).

  The clearest feature of the bar-chart is that the configuration benefiting the most from the implementation of a pitch-regulated mechanism is the *PD50* one. As for the discussions concerning Figures 14 and 15, the effects increase exponentially with the coverage area, with the steepest variations occurring between $10-60\%$ and saturating afterwards. In the worst-case scenario, namely at a coverage area of 100%, the effect of implementing a pitch-regulated mechanism can enhance the AEP by 70% for the *PD50* configuration, when compared to its *SR* counterpart. The values for the *Bare* configuration are not as high but, nonetheless, they achieve an AEP improvement above 40%, which constitutes a non-negligible value altogether.

  The second feature to be highlighted is that the effects of the pitch-regulation mode upon the *Bare* and *PD50* configurations contrast noticeably with the ones observed for the *PD25* layout. In the latter case, the AEP enhancement does not surpass the 5% value regardless of the coverage area. The only case in which it reaches the 10% threshold is for the *Clean* paradigm which, as known, does not correspond to realistic flow conditions.

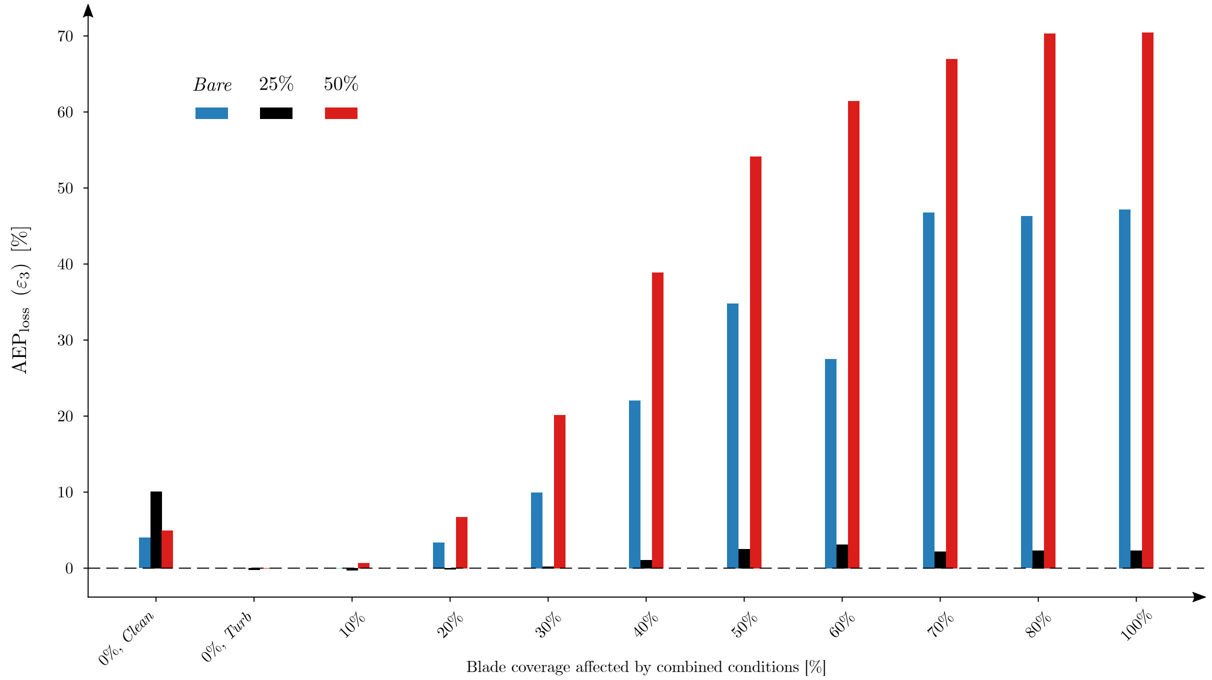

Figure 16. ε_2 loss factor for the *Bare*, *PD25* and *PD50* configurations simulated at different coverage areas.

Once again, the explanation for the observed differences is to be found in the discussion about the aerodynamic curves undertaken in Section 4.1 and, more concretely, in the features observed in Figure 10b. As shown there, the *PD25* configuration achieves to extend the angular region for which the aerodynamic efficiency stands at relatively high values, whereas the *Bare* and *PD50* cases stall abruptly. Seemingly, the pitch-regulation control enables the latter two configurations to remain near the peak of the efficiency curve, which redounds to a relative AEP gain. Instead, such a pitch regulation does not have as clear an effect upon the *PD25* configuration, given its flatter morphology in the saturation and pre-stalling zone.

From the discussion above, it is apparent that the decision for implementing a pitch-regulated control is made upon different considerations depending on the particular configuration of the turbine. In the case of the *Bare* and *PD50* layouts, a *PR* mode induces a relative AEP gain, whereas that is not the case for the *PD25* configuration.

The point is that, according to ε_2, the implementation of *PD*s makes sense, merely, if the *PD25* layout is considered. Accordingly, the above reasoning allows decoupling the roles played by the *PD* elements, on the one hand, and the pitch-regulation mechanism, on the other hand, based on their functionality. Indeed, the *PD*s would act as a flow-control technique that achieves to mitigate the AEP loss at moderate-to-high coverage areas, as long as they are arranged following the *PD25* layout, whereas the pitch-regulation mechanism would show a minor impact on the AEP enhancement.

https://doi.org/10.5194/wes-2025-36
Preprint. Discussion started: 8 April 2025

5 CONCLUSIONS

The purpose of the study undertaken herein has been twofold: the first has focused on analysing the aerodynamic behaviour of a transitionally-operating airfoil considering three configurations, namely a plain NACA0021 geometry (*Bare*) and the same geometry equipped with different distributions of a *PD*-based flow-control technique, positioned at the 25% of the chordal length downstream the leading-edge (*PD25* configuration) and at the 50% of it (*PD50*). Such configurations are tested under a set of different flow-paradigms (*Clean*, *Turbulent* and *Combined*) and Reynolds numbers (Re$\in [0.8, 1.2] \times 10^5$). As mentioned in Section 1, the study by no means attempts to reproduce realistic conditions in full detail, neither on the airfoil geometry being tested nor on the wind-tunnel flow. Rather, it wishes to convey the idea that trying to reproduce such realistic conditions is sufficiently relevant, insofar it has an impact on the power production estimation of a system. Regardless of the relevance that the outlined procedure may have, there are certain aspects of its implementation in the current experimental set-up that could be improved. Such limitations are remarked below as potential fronts in which improvements could be made:

- The technical limitations of the tunnel do not allow achieving Reynolds numbers above 1.2×10^5, as the motors employed for displacing the probes throughout the test-section are not powerful enough for overcoming the aerodynamic loads exerted upon the probes.
- The angular range of the experiments has been limited to 20° due to the excessive blockage of the airfoil for larger angles. Blockage corrections have been applied according to, which may mitigate the spurious effects to some extent but, still, angles-of-attack larger than 20° lead to overly poor data. On this respect, the need for an extrapolation is insurmountable, as the BEM code requires the extension of the polars to 360° as an input. However, the angular range of 20° corresponds to an interval large enough for covering the typical operation conditions of the wind-turbine. The extrapolation is known to homogenize the curves in the post-stall region. This does not mean that the evolution of the polars beyond stall is irrelevant. Such an extrapolation does play a role, albeit a minor one, on the variations observed in the final power curves and, correspondingly, in the estimated AEP values.
- The NACA0021 employed corresponds to a standard geometry, not an optimized one used in current wind-turbine systems. A possible future line is to devise 3D-printing-based fabrication procedure robust enough for manufacturing arbitrary aerodynamic geometries on demand. Meanwhile, though, the NACA0021 geometry is employed as an application-agnostic model, which means that it serves the purpose of showing that turbulence and roughness effects do, in fact, manifest in the experiments. Although the quantitative values obtained experimentally may be relevant enough, the extension of such values to a hypothetical wind-turbine system must, in any case, be interpreted in qualitative terms.
- The sand-grain paper employed as a roughness pattern shows the advantage of being both easily applicable and removable. Even though it constitutes a standard experimental procedure, the technique does not emulate the stochastic roughness distributions and sizes encountered in real systems. The point mentioned with respect to the 3D-printing procedure applies equally to this one. Indeed, the development of a 3D-printing fabrication technique could allow substituting the sand-grain paper with integrated surface defects, which is the next level of approximation with respect to roughness.

- What has been said with respect to the stochastic roughness serves equally when it comes to the *PD*s. The fact of having chosen such a method relies, basically, on the versatility of its implementation. The parameters of the distributions, mainly the shape of the elements and their height, call for a proper characterization and optimization. For further details on the choosing and a first characterization of the *PD*s, the reader is referred to Zarketa-Astigarraga.

Despite the limitations, the findings of the aerodynamic analysis carried out upon the NACA0021 geometry may be considered qualitatively relevant:

- The over-prediction of the aerodynamic behaviour performed under *Clean* conditions calls for a testing of wind-turbine blades subjected to flow paradigms that are as realistic as possible.
- The effects of the *PD*-based distributions upon the aerodynamic behaviour of the blades do not follow a well-established trend, neither for the *Clean* nor for the *Combined* paradigms, and such effects are strongly Reynolds dependent. On this respect, a better-suited flow-control technique may be one based on an active mechanism that allows adapting the controlling configuration to the conditions on the incoming flow, rather than a passive technique as the one employed herein.
- The inability to explain the physical mechanisms behind the observed variations calls for a more thorough research on the analysed configurations, employing other measurement techniques such as surface-pressure measurements or oil-flow visualizations Zarketa-astigarraga et al. (2022); Zarketa-Astigarraga et al. (2023). The more local nature of those techniques may shed light upon the processes that underlie the several lift- and efficiency-enhancements observed throughout the multi-parametric field, which the global scope of c_l and c_d measurements conceal.
- Although the study has focused on a specific SHAWT device operating under transitional flows, both the experimental methodology and the numerical approach outlined herein are transferable to differently sized systems such as large-scale wind-turbines.

The second goal of the study has been to translate the impacts that the different configurations, flow-paradigms and Reynolds numbers have on the aerodynamic curves to the overall system of a particular SHAWT. On this respect, the analysis has shown that:

- The variations of the power curves and the AEP estimations with the coverage area strongly depend on both the flow-paradigm (*Clean*, *Turbulent* and *Combined*) and the blade configuration (*Bare*, *PD25* or *PD50*).
- The global trend of the AEP variations shows a progressive loss with the coverage area, and evolves in an exponential manner whereby the strongest variations occur during the $10-50\%$ coverage due to the larger contribution of the outermost blade sections, saturating afterwards.
- The *PD25* configuration is shown to be the only one enhancing the AEP with respect to its *Bare* counterpart, but solely at moderate-to-high coverage areas (>30%). The relative AEP improvement can reach values as high as 80% in the worst-case scenario.

- The pitch-regulation control is effective in enhancing the AEP, majorly, in the case of the *Bare* and *PD50* configurations, reaching relative AEP improvements of 40 and 70%, respectively.
- A joint interpretation of the AEP losses induced by the *PD* elements, on the one hand, and the pitch-regulation mechanism, on the other hand, allows deducing that choosing the *PD25* configuration is beneficial for improving the AEP at high coverage areas, whereas implementing a pitch-regulated control shows a minor effect on it.
- The results show that the two flow-control methods implemented in the study, namely the *PD*s and the pitch-regulation, require a joint consideration for achieving the optimal configuration of the blades in terms of AEP enhancement.

. 6 Author contributions

- A. Zarketa-Astigarraga: Conceptualization, Methodology, Software, Validation, Formal Analysis, Investigation, Data Curation, Writing – Original draft, Writing – Review & Editing, Visualization.
- U. Arrieta-Lizarazu: Conceptualization, Methodology, Software, Validation, Formal Analysis, Investigation, Data Curation, Writing – Original draft, Writing – Review & Editing, Visualization.
- M. Penalba: Conceptualization, Methodology, Resources, Writing – Original draft, Writing – Review & Editing, Supervision, Project Administration, Funding Acquisition.
- A. Martin-Mayor: Conceptualization, Methodology, Resources, Writing – Review & Editing, Supervision, Project Administration, Funding Acquisition.
- M. Martinez-Agirre: Conceptualization, Methodology, Resources, Writing – Review & Editing, Supervision, Project Administration, Funding Acquisition.

. 7 Competing interests

The authors state that no conflicts of interests with other institutions have taken place during the elaboration of the submitted manuscript.

. 8 Acknowledgements

The authors gratefully acknowledge the financial support from the Department of Education of the Basque Government for the Research Grant [PRE_2017_1_0178] and the Research Group [No. IT1505-22].

References

LabVIEW Software main page, https://www.ni.com/en-us/shop/labview.html, a.

QBlade code main page, http://www.q-blade.org/, b.

AWEA Small Wind Turbine Global Market Study, Tech. rep., American Wind Energy Association (AWEA), 2010.

Renewable Capacity Statistics 2022, Tech. rep., International Renewable Energy Agency (IRENA), 2022.

Aksoy, M. H.: Flow characteristics and passive flow control of circular cylinders with triangular vortex generators: An experimental investigation, 142, 103 836, https://doi.org/10.1016/j.apor.2023.103836.

Amirzadeh, B., Louhghalam, A., Raessi, M., and Tootkaboni, M.: A computational framework for the analysis of rain-induced erosion in wind turbine blades, part I: Stochastic rain texture model and drop impact simulations, Journal of Wind Engineering and Industrial Aerodynamics, 163, 33–43, https://doi.org/10.1016/j.jweia.2016.12.006, 2017.

Ananda, G., Sukumar, P., and Selig, M.: Measured Aerodynamic Characteristics of Wings at Low Reynolds Numbers, Aerospace Science and Technology, 42, 392–406, https://doi.org/10.1016/j.ast.2014.11.016, 2015.

Arumugam, P., Ramalingam, V., and Bhaganagar, K.: A pathway towards sustainable development of small capacity horizontal axis wind turbines – Identification of influencing design parameters & their role on performance analysis, Sustainable Energy Technologies and Assessments, 44, 101 019, https://doi.org/10.1016/j.seta.2021.101019, 2021.

Ashuri, T., Martins, J. R., Zaaijer, M. B., van Kuik, G. A., and van Bussel, G. J.: Aeroservoelastic design definition of a 20 MW common research wind turbine model, Wind energy, 19, 2071–2087, https://doi.org/10.1002/we.1970, 2016.

Bartolomé, L. and Teuwen, J.: Prospective challenges in the experimentation of the rain erosion on the leading edge of wind turbine blades, Wind Energy, 22, 140–151, https://doi.org/10.1002/we.2272, 2019.

Bianchini, A., Bangga, G., Baring-Gould, I., Croce, A., Cruz, J. I., Damiani, R., Erfort, G., Simao Ferreira, C., Infield, D., Nayeri, C. N., Pechlivanoglou, G., Runacres, M., Schepers, G., Summerville, B., Wood, D., and Orrell, A.: Current status and grand challenges for small wind turbine technology, Wind Energy Science Discussions, 2022, 1–54, https://doi.org/10.5194/wes-7-2003-2022, 2022.

Bons, J. P.: A Review of Surface Roughness Effects in Gas Turbines, 132, 021 004, https://doi.org/10.1115/1.3066315.

Caliskan, S., Sevik, S., and Ozdilli, O.: Heat transfer enhancement by a sinusoidal wavy plate having punched triangular vortex generators, 181, 107 769, https://doi.org/10.1016/j.ijthermalsci.2022.107769.

Chini, S. F., Mahmoodi, M., and Nosratollahi, M.: The Potential of Using Superhydrophobic Surfaces on Airfoils and Hydrofoils: a Numerical Approach, International Journal of Computational Materials Science and Surface Engineering, 7, 44, https://doi.org/10.1504/IJCMSSE.2017.088726, 2017.

Cho, S.: Control of a flow around a low Reynolds number airfoil using longitudinal strips, Ph.D. thesis, Seoul National University, Seoul, South Corea, 2019.

Corten, G. P. and Veldkamp, H. F.: Aerodynamics: Insects can halve wind-turbine power, Nature, 412, 41–42, 2001.

Curci, R., Bruno, P., and Carmo, S.: Analysis of wind turbine blade aerodynamic optimization strategies considering surface degradation, Journal of the Brazilian Society of Mechanical Sciences and Engineering, 43, 1–22, https://doi.org/10.1007/s40430-021-03166-3, 2021.

Dean, B. and Bhushan, B.: Shark-skin surfaces for fluid-drag reduction in turbulent flow: A review, Philosophical Transactions of the Royal Society A: Mathematical, Physical and Engineering Sciences, 368, 4775–4806, https://doi.org/10.1098/rsta.2010.0201, 2010.

Du, L., Berson, A., and Dominy, R. G.: Aerofoil behaviour at high angles of attack and at Reynolds numbers appropriate for small wind turbines, Proceedings of the Institution of Mechanical Engineers, Part C: Journal of Mechanical Engineering Science, 229, 2007–2022, https://doi.org/10.1177/0954406214550016, 2015.

Flack, K. A., Schultz, M. P., and Barros, J. M.: Skin Friction Measurements of Systematically-Varied Roughness: Probing the Role of Roughness Amplitude and Skewness, 104, 317–329, https://doi.org/10.1007/s10494-019-00077-1.

Gao, L., Zhang, H., Liu, Y., and Han, S.: Effects of vortex generators on a blunt trailing-edge airfoil for wind turbines, Renewable Energy, 76, 303–311, https://doi.org/10.1016/j.renene.2014.11.043, 2015.

Gaster, M.: The Role of Spatially Growing Waves in the Theory of Hydrodynamic Stability, Progress in Aerospace Sciences, 6, 251–270, 1965.

Gaster, M.: The Structure and Behaviour of Laminar Separation Bubbles, 1967.

Gaster, M.: Growth of Disturbances in Both Space and Time, Physics of Fluids, 11, 723, 1968.

Glauert, H.: Airplane Propellers, Springer Berlin Heidelberg, Berlin, Heidelberg, 1935.

Habali, S. M. and Saleh, I. A.: Local design , testing and manufacturing of small mixed airfoil wind turbine blades of glass fiber reinforced plastics Part I : Design of the blade and root, Energy Conversion & Management, 41, 249–280, https://doi.org/10.1016/S0196-8904(99)00103-X, 2000.

Hamlaoui, M. N., Smaili, A., Dobrev, I., Pereira, M., Fellouah, H., and Khelladi, S.: Numerical and experimental investigations of HAWT near wake predictions using Particle Image Velocimetry and Actuator Disk Method, Energy, 238, 121 660, https://doi.org/10.1016/j.energy.2021.121660, 2022.

Han, W., Kim, J., and Kim, B.: Effects of contamination and erosion at the leading edge of blade tip airfoils on the annual energy production of wind turbines, Renewable Energy, 115, 817–823, https://doi.org/10.1016/j.renene.2017.09.002, 2018.

Hansen, K., Kelso, R. M., Choudhry, A., and Arjomandi, M.: Laminar Separation Bubble Effect on the Lift Curve Slope of an Airfoil, in: 19th Australasian Fluid Mechanics Conference.

Hansen, M. O. L., Velte, C. M., ØYe, S., Hansen, R., Sørensen, N. N., Madsen, J., and Mikkelsen, R.: Aerodynamically shaped vortex generators, Wind Energy, 18, 1875–1891, https://doi.org/10.1002/we.1842, 2015.

Hultgren, L. S. and Ashpis, D. E.: Demonstration of separation control using dielectric barrier discharge plasma actuators, AIAA Journal, 56, 4614–4620, https://doi.org/10.2514/1.J056976, 2018.

Karthikeyan, N., Sudhakar, S., and Suriyanarayanan, P.: Experimental studies on the effect of leading edge tubercles on laminar separation bubble, in: 52nd Aerospace Sciences Meeting, January, pp. 1–16, American Institute for Aeronautics and Astronautics (AIAA), National Harbor, MA, U.S.A, https://doi.org/10.2514/1.J058294, 2014.

KC, A., Whale, J., and Urmee, T.: Urban wind conditions and small wind turbines in the built environment: A review, Renewable Energy, 131, 268–283, https://doi.org/10.1016/j.renene.2018.07.050, 2019.

Kc, A., Whale, J., Evans, S. P., and Clausen, P. D.: An investigation of the impact of wind speed and turbulence on small wind turbine operation and fatigue loads, Renewable Energy, 146, 87–98, https://doi.org/10.1016/j.renene.2019.06.124, 2020.

KC, A., Whale, J., and Peinke, J.: An investigation of the impact of turbulence intermittency on the rotor loads of a small wind turbine, Renewable Energy, 169, 582–597, https://doi.org/10.1016/j.renene.2021.01.049, 2021.

Khalfallah, M. G. and Koliub, A. M.: Effect of dust on the performance of wind turbines, Desalination, 209, 209–220, https://doi.org/10.1016/j.desal.2007.04.030, 2007.

Kok, M. and Young, T. M.: The evaluation of hierarchical structured superhydrophobic coatings for the alleviation of insect residue to aircraft laminar flow surfaces, Applied Surface Science, 314, 1053–1062, https://doi.org/10.1016/j.apsusc.2014.06.039, 2014.

Latoufis, K., Riziotis, V., Voutsinas, S., and Hatziargyriou, N.: Effects of Leading Edge Erosion on the Power Performance and Acoustic Noise Emissions of Locally Manufactured Small Wind Turbine Blades, Journal of Physics: Conference Series, 1222, 1–12, https://doi.org/10.1088/1742-6596/1222/1/012010, 2019.

Law, H. and Koutsos, V.: Leading edge erosion of wind turbines: Effect of solid airborne particles and rain on operational wind farms, Wind Energy, 23, 1955–1965, https://doi.org/10.1002/we.2540, 2020.

Li, X., Zhang, L., Song, J., Bian, F., and Yang, K.: Airfoil design for large horizontal axis wind turbines in low wind speed regions, 145, 2345–2357, https://doi.org/10.1016/j.renene.2019.07.163.

Maldonado, V., Castillo, L., Thormann, A., and Meneveau, C.: The role of free stream turbulence with large integral scale on the aerodynamic performance of an experimental low Reynolds number S809 wind turbine blade, Journal of Wind Engineering and Industrial Aerodynamics, 142, 246–257, https://doi.org/10.1016/j.jweia.2015.03.010, 2015.

Manwell, J. F., McGowan, J. G., and Rogers, A. L.: Wind Energy Explained Theory, Design and Application, Wiley & Sons, 2 edn., 2011.

Martini, M., Guanche, R., Losada, I. J., and Vidal, C.: Accessibility assessment for operation and maintenance of offshore wind farms in the North Sea, Wind Energy, pp. 1–20, https://doi.org/10.1002/we.2028, 2016.

Meng, X., Hu, H., Yan, X., Liu, F., and Luo, S.: Lift improvements using duty-cycled plasma actuation at low Reynolds numbers, Aerospace Science and Technology, 72, 123–133, https://doi.org/10.1016/j.ast.2017.10.038, 2018.

Meseguer-Ruiz, J. and Sanz-Andrés, Á.: Procedimientos para determinar numéricamente la resistencia, in: Aerodinámica Básica, chap. 9.2, pp. 262–264, Garceta Grupo Editorial, 2 edn., 2012.

Mishnaevsky, L. J.: Repair of wind turbine blades : Review of methods and related computational mechanics problems, Renewable Energy, 140, 828–839, https://doi.org/10.1016/j.renene.2019.03.113, 2019.

Mohamed Elhadi, I. and Mamoun, M.: Water Droplet Erosion of Wind Turbine Blades: Mechanics, Testing, Modeling and Future Perspectives, Materials, 13, 1 – 33, https://doi.org/10.3390/ma13010157, 2020.

Moreira Chagas, C. C., Giannini Pereira, M., Pinguelli Rosa, L., Fidelis da Silva, N., Vasconcelos Freitas, M. A., and Hunt, J. D.: From Megawatts to Kilowatts: A Review of Small Wind Turbine Applications, Lessons From The US to Brazil, Sustainability, 12, 1–25, https://doi.org/10.3390/su12072760, 2020.

Mueller-Vahl, H., Pechlivanoglou, G., Nayeri, C. N., and Paschereit, C. O.: Vortex generators for wind turbine blades: a combined wind tunnel and wind turbine parametric study, in: Proceedings of ASME Turbo Expo 2012, pp. 1–16, ASME, https://doi.org/10.1115/GT2012-69197, 2012.

Orrell, A., Preziuso, D., Foster, N., Morris, S., and Homer, J.: 2018 Distributed Wind Market Report, Tech. rep., U.S. Department of Energy, office of Energy Efficiency & Renewable Energy, 2018.

Ozçakmak, O. S., Madsen, H. A., Sørensen, N. N., Sorensen, J. N., Fischer, A., and Bak, C.: Inflow Turbulence and Leading Edge Roughness Effects on Laminar-Turbulent Transition on NACA 63-418 Airfoil, 1037, 022 005, https://doi.org/10.1088/1742-6596/1037/2/022005.

Pagnini, L. C., Burlando, M., and Repetto, M. P.: Experimental power curve of small-size wind turbines in turbulent urban environment, Applied Energy, 154, 112–121, https://doi.org/10.1016/j.apenergy.2015.04.117, 2015.

Panta, A., Mohamed, A., Marino, M., Watkins, S., and Fisher, A.: Unconventional control solutions for small fixed wing unmanned aircraft, Progress in Aerospace Sciences, 102, 122–135, https://doi.org/10.1016/j.paerosci.2018.07.005, 2018.

Reshotko, E.: Boundary-Layer Stability and Transition, 8, 311–349, https://doi.org/10.1146/annurev.fl.08.010176.001523.

Ricci, R. and Montelpare, S.: Analysis of Boundary Layer Separation Phenomena by Infrared Thermography Use of Acoustic and/or Mechanical Devices to Avoid or Reduce the Laminar Separation Bubble Effects, Quantitative InfraRed Thermography Journal, 6, 101–125, https://doi.org/10.1016/j.expthermflusci.2005.08.007, 2009.

Ricci, R., Montelpare, S., and Silvi, E.: Study of Acoustic Disturbances Effect on Laminar Separation Bubble by IR Thermography, Experimental Thermal and Fluid Science, 31, 349–359, 2007.

Ricci, R., Montelpare, S., and Renzi, E.: Study of Mechanical Disturbances Effects on the Laminar Separation Bubble by Means of Infrared Thermography, International Journal of Thermal Sciences, 50, 2091–2103, https://doi.org/10.1016/j.ijthermalsci.2011.05.013, 2011.

Ruggiero, S., Varho, V., and Rikkonen, P.: Transition to distributed energy generation in Finland : Prospects and barriers, Energy Policy, 86, https://doi.org/10.1016/j.enpol.2015.07.024, 2015.

Sareen, A., Deters, R. W., Henry, S. P., and Selig, M. S.: Drag Reduction Using Riblet Film Applied to Airfoils for Wind Turbines, Journal of Solar Energy Engineering, 136, 021 007, https://doi.org/10.1115/1.4024982, 2013.

Schlichting, H. and Gersten, K.: Fundamentals of Boundary-Layer Theory, in: Boundary-Layer Theory, pp. 29–49, Springer Berlin Heidelberg.

Shahinfar, S., Sattarzadeh, S., Fransson, J., and Talamelli, A.: Revival of Classical Vortex Generators now for Transition Delay, Physical Review Letters, 109, 1–5, https://doi.org/10.1103/PhysRevLett.109.074501, 2012.

Srivastava, K. and Sahoo, R. R.: Experimental and numerical study on thermal performance of new envelope and triangular vortex generators with different pitch and angle of attack, 49, 102 459, https://doi.org/10.1016/j.tsep.2024.102459.

Sunderland, K., Woolmington, T., Blackledge, J., and Conlon, M.: Small wind turbines in turbulent (urban) environments : A consideration of normal and Weibull distributions for power prediction, Jnl. of Wind Engineering and Industrial Aerodynamics, 121, 70–81, https://doi.org/10.1016/j.jweia.2013.08.001, 2013.

Thompson, M., Watkins, S., White, C., and Holmes, J.: Span-wise wind fluctuations in open terrain as applicable to small flying craft, 115, 693–701, https://doi.org/10.1017/S0001924000006412.

Torrano, I.: Low speed wind tunnel design, setup, validation and testing of airfoils in turbulent in ow conditions, Ph.D. thesis, Mondragon Goi Eskola Politeknikoa, 2016.

Torres-Madroñero, J. L., Alvarez-Montoya, J., Restrepo-Montoya, D., Tamayo-Avendaño, J. M., Nieto-Londoño, C., and Sierra-Pérez, J.: Technological and operational aspects that limit small wind turbines performance, Energies, 13, 1–39, https://doi.org/10.3390/en13226123, 2020.

Tuller, S. E. and Brett, A. C.: The Characteristics of Wind Velocity that Favor the Fitting of a Weibull Distribution in Wind Speed Analysis, Journal of Climate and Applied Meteorology, 23, 124–134, https://doi.org/10.1175/1520-0450(1984)023<0124:TCOWVT>2.0.CO;2, 1983.

Tummala, A., Kishore, R., Kumar, D., and Indraja, V.: A review on small scale wind turbines, Renewable and Sustainable Energy Reviews, 56, 1351–1371, https://doi.org/10.1016/j.rser.2015.12.027, 2020.

Viterna, L. A. and Corrigan, R. D.: Fixed Pitch Rotor Performance of Large Horizontal Axis Wind Turbines, Tech. rep., NASA, Cleveland, Ohio, USA, 1982.

Waloddi Weibull, B.: A Statistical Distribution Function of Wide Applicability, Journal of Applied Mechanics, Vol. 18, 293–297, https://doi.org/10.1115/1.4010337, 1951.

Watkins, S., Burry, J., Mohamed, A., Marino, M., Prudden, S., Fisher, A., Kloet, N., Jakobi, T., and Clothier, R.: Ten questions concerning the use of drones in urban environments, 167, 106 458, https://doi.org/10.1016/j.buildenv.2019.106458, a.

Watkins, S., Milbank, J., Loxton, B. J., and Melbourne, W. H.: Atmospheric Winds and Their Implications for Microair Vehicles, 44, 2591–2600, https://doi.org/10.2514/1.22670, b.

Wekesa, D. W., Wang, C., Wei, Y., and Zhu, W.: Experimental and numerical study of turbulence effect on aerodynamic performance of a small-scale vertical axis wind turbine, Journal of Wind Engineering and Industrial Aerodynamics, 157, 1–14, https://doi.org/10.1016/j.jweia.2016.07.018, 2016.

Yarusevych, S. and Kotsonis, M.: Effect of Local DBD Plasma Actuation on Transition in a Laminar Separation Bubble, Flow, Turbulence and Combustion, 98, 195–216, https://doi.org/10.1007/s10494-016-9738-1, 2017.

Zamiri, A., You, S. J., and Chung, J. T.: Surface roughness effects on film-cooling effectiveness in a fan-shaped cooling hole, 119, 107 082, https://doi.org/10.1016/j.ast.2021.107082.

Zarketa-Astigarraga, A.: Aerodynamic Characterization of Transitionally-operating Airfoils under a set of Flow Conditions going from Ideal to Real Configurations.

Zarketa-Astigarraga, A., Martin-Mayor, A., and Martinez-Agirre, M.: Experimental uncertainty decompositions of aerodynamic coefficients affected by operative condition variations, Measurement, 165, 1–14, https://doi.org/10.1016/j.measurement.2020.107941, 2020a.

Zarketa-Astigarraga, A., Martin-Mayor, A., and Martinez-Agirre, M.: Theoretical concepts for describing a replication-levels-based uncertainty analysis approach, in: Advances in Measurements and Instrumentation: Reviews, Book Series, Vol. 2, edited by Yurish, S., IFSA Publishing, 1 edn., 2020b.

Zarketa-Astigarraga, A., Martin-Mayor, A., Martinez-Agirre, M., and Peñalba-Retes, M.: Assessing the statistical validity of momentum-deficit-based C_D measurements in turbulent configurations, Measurement, 181, https://doi.org/10.1016/j.measurement.2021.109592, 2021.

Zarketa-astigarraga, A., Penalba, M., Martin-mayor, A., and Martinez-agirre, M.: Experimental assessment of scale-effects on the aerodynamic characterization of a transitionally-operating airfoil working under clean flow conditions, Measurement, 188, 110 414, https://doi.org/10.1016/j.measurement.2021.110414, 2022.

Zarketa-Astigarraga, A., Penalba, M., Martin-Mayor, A., and Martinez-Agirre, M.: Impact of turbulence and blade surface degradation on the annual energy production of small-scale wind turbines, Wind Energy, https://doi.org/10.22541/au.167848404.41193767/v1, in press, 2023.

Zhao, F. and Hutchinson, M.: GLOBAL WIND REPORT 2023, Tech. rep., Global Wind Energy Council (GWEC), 2023.